Monthly Notices of the ROYAL ASTRONOMICAL SOCIETY

MNRAS **520,** 3201–3217 (2023) https://doi.org/10.1093/mnras/stac2104
Advance Access publication 2022 July 28

The magnetic field of the chemically peculiar star V352 Peg

L. Fréour [1,2,3]★ C. Neiner [1] J. D. Landstreet [4,5] C. P. Folsom [6] and G. A. Wade[7]

[1]*LESIA, Paris Observatory, PSL University, CNRS, Sorbonne University, Université de Paris, 5 place Jules Janssen, F-92195 Meudon, France*
[2]*Central School of Nantes, 1 rue de la Noë, F-44300 Nantes, France*
[3]*Technical University of Denmark, Anker Engelunds Vej 1 Bygning 101A, 2800 Kgs. Lyngby, Denmark*
[4]*University of Western Ontario, Department of Physics & Astronomy, London, Ontario N6A 3K7, Canada*
[5]*Armagh Observatory and Planetarium, College Hill, Armagh BT61 9DG, Northern Ireland, UK*
[6]*University of Tartu, Faculty of Science and Technology, Tartu Observatory, 50090 Tartu, Estonia*
[7]*Dept. of Physics & Space Science, Royal Military College of Canada, PO Box 17000 Station Forces, Kingston, ON K7K 0C6, Canada*

Accepted 2022 July 20. Received 2022 July 20; in original form 2021 July 23

ABSTRACT

We present a spectropolarimetric analysis of the hot star V352 Peg. We have acquired 18 spectropolarimetric observations of the star with ESPaDOnS at the CFHT between 2018 and 2019 and completed our data set with one archival ESPaDOnS measurement obtained in 2011. Our analysis of the spectra shows that the star is on the main sequence and chemically peculiar, i.e. it is a Bp star, with overabundances of iron peak elements (Ti, Cr, and Fe) and underabundance of He and O. Through a Least-Square Deconvolution of each spectrum, we extracted the mean Zeeman signature and mean line profile of thousands of spectral lines and detected a magnetic field in V352 Peg. By modelling the Stokes I and V profiles and using the Oblique Rotator Model, we determined the geometrical configuration of V352 Peg. We also performed Zeeman–Doppler Imaging (ZDI) to provide a more detailed characterization of the magnetic field of V352 Peg and its surface chemical distributions. We find a magnetic field that is mainly dipolar, dominantly poloidal, and largely non-axisymmetric with a dipole field strength of ∼9 kG and a magnetic axis almost perpendicular to the rotation axis. The strong variability of Stokes I profiles also suggests the presence of chemical spots at the stellar surface.

Key words: techniques: polarimetric – stars: chemically peculiar – stars: individual: V352 Peg – stars: magnetic field.

1 INTRODUCTION

Magnetic fields are known to exist in about 10 per cent of hot stars on the main sequence. Recent projects and international collaborations, among which the Magnetism in Massive Stars (MiMeS; Wade et al. 2016) and the Large Impact of magnetic Fields on the Evolution (LIFE) of hot stars (Martin et al. 2018) programmes, have enabled researchers to progress in the understanding of magnetism.

Contrary to cool stars, hot stars exhibit a radiative envelope where a solar-like dynamo cannot arise. The magnetic field present in hot stars is believed to have a fossil origin, most likely a remnant of the magnetic field of the molecular cloud where the star formed (Moss 2001; Neiner et al. 2014, and references therein) or of the field generated during the convective phase of the pre-main sequence (Alecian et al. 2019, and references therein), or possibly resulting from a merger (Schneider et al. 2016). A high percentage of magnetic hot stars also exhibit inhomogenous surface distribution of chemical elements and are classified as chemically peculiar (CP). Through atomic diffusion, chemical elements, channelled by the magnetic field lines, gather in spots distributed around the stellar surface (Michaud, Mégessier & Charland 1981). Reconstructing the magnetic field and surface distribution of chemical elements of such stars can help understanding the interaction between chemical elements and magnetic field.

V352 Peg (= HD 221218, HIP 115991) is an α^2 CVn type of star, first detected as a photometrically variable star by the *Hipparcos* mission (Perryman et al. 1997). It has been classified as a B8/9III star in the *Hipparcos* and Skiff catalogs (Skiff 2014), thus as an evolved hot star. However, more recent observations obtained for the Revised TESS Input Catalog (TIC; Stassun et al. 2019) classified V352 Peg as a dwarf star.

Here, we present high-resolution spectropolarimetric observations of V352 Peg (Section 2). We determine the physical parameters of the star (Section 3.1) and its chemical composition (Section 3.2). We then perform a spectropolarimetric analysis (Section 4) to check for the presence of a magnetic field and determine its strength and geometrical configuration using a Zeeman–Doppler Imaging (ZDI) code developed by Folsom et al. (2018). We also produce chemical maps of the most abundant elements. Finally, our results and hypotheses are discussed in Section 5.

2 OBSERVATIONS

Seventeen observations of V352 Peg were collected between 2019 August 17 and June 11, within the scope of the LIFE project. An archival observation obtained on the 2011 August 19, as part of the MiMeS international program is also available. All the observations were taken with the ESPaDOnS spectropolarimeter at the Canada-

★ E-mail: laurane.freour@univie.ac.at

© The Author(s) 2022.
Published by Oxford University Press on behalf of Royal Astronomical Society. This is an Open Access article distributed under the terms of the Creative Commons Attribution License (http://creativecommons.org/licenses/by/4.0/), which permits unrestricted reuse, distribution, and reproduction in any medium, provided the original work is properly cited.

Downloaded from https://academic.oup.com/mnras/article/520/3/3201/6651394 by CNRS user on 11 April 2023

France-Hawaii Telescope (CFHT) and cover a large wavelength range, from 370 to 1040 nm, with a spectral resolution of 65 000.

Each observation consists of four subexposures, each of them taken in a specific polarimeter configuration. The data reduction pipeline of ESPaDOnS is Libre-Esprit (Donati 1997) included in the UPENA package. We normalized the spectra through a semi-automatic PYTHON code (Martin 2017). The signal-to-noise ratio (S/N) of the spectra ranges from 143 to 537 with an average value of 376, measured at 503 nm. Relevant information regarding the observations is gathered in Table 1. Note that, when checking the night reports from the CFHT, we noticed large differences in the S/N between subexposures for the observation #2 (2297769). This is not the case for the other observations and could be the evidence of some transient (unknown) issue. There are no obvious systematic errors in the observation so we decided to keep it in the longitudinal magnetic field analysis. However, the ZDI is more sensitive to small details in line profiles and we rejected observation #2 from that analysis, since it does not have a significant impact on the rotation phase coverage.

The circular polarization (Stokes V) and null spectra N are computed by respectively constructive and destructive combination of the four polarimetric subexposures. The total intensity (Stokes I) is also extracted.

3 STELLAR PARAMETERS

3.1 Fundamental parameters

First estimates of the physical parameters (effective temperature $T_{\rm eff}$, luminosity L, gravity $\log g$, radius R, and mass M) of V352 Peg were obtained from the TIC (Stassun et al. 2019), based on Gaia DR2 colours and distance. These data are presented in Table 2. Only the error on the effective temperature is available in the TIC. We computed the error on the radius by propagating the errors on Gaia distance D, Gaia magnitude G, and $T_{\rm eff}$ in equation (4) from Stassun et al. (2019). The mass is computed using a unified spline relation between the effective temperature and the mass. The corresponding nodal points are presented in table 5 of Stassun et al. (2019). The uncertainty in the mass is then calculated by propagating the error on $T_{\rm eff}$ in the spline function. Finally, we estimated the errors on the luminosity and the surface gravity by propagating the errors from the above mentioned parameters in the formula used by Stassun et al. (2019).

As a check on the fundamental parameters provided in the TIC, we retrieved the Geneva six-colour photometry for this star from the Lausanne General Catalog of Photometric Data (Mermilliod, Mermilliod & Hauck 1997), which is maintained online at the Masaryk University in Brno, Czech Republic.[1] (No Strömgren photometry of this star appears to be available.) These data were used to obtain values of $T_{\rm eff} = 11376 \pm 57$ K and $\log g = 4.22 \pm 0.08$, employing the program CALIB.F (Künzli et al. 1997), as described in more detail by Silaj & Landstreet (2014). The underlying calibrations for fundamental parameters derived from Geneva photometry with CALIB.F are described by Künzli et al. (1997). As we will show in Section 3.2, V352 Peg is a CP star. CALIB.F does not include options for CP stars, but it does allow the user to choose an overall atmospheric abundance of solar, or of solar enhanced or diminished by 1 dex. We have used the +1 dex enhanced calibrations, but the result changes the computed value of $T_{\rm eff}$ from that of a solar abundance star by only about 100 K, and $\log g$ changes by only about 0.02 dex. The uncertainties reported by CALIB.F are fitting uncertainties, which we have replaced with larger uncertainties that we consider to be more realistic for ApBp stars. The agreement of the values obtained from Geneva photometry with that found in the TIC catalog is satisfactory, but we suggest that the TIC uncertainties may be somewhat underestimated for this CP star. From the gravity values, it is clear that (in spite of luminosity classification III) V352 Peg is a main sequence star.

The rotation period determined from the more than 140 photometric observations obtained by *Hipparcos* (ESA 1997) is reported in various online versions of the *Hipparcos* variability catalog[2] to be either $P_{\rm rot} = 2.64$ or 2.63641 ± 0.00006 d. This photometric period will be considerably improved below; Table 2 reports our final value.

Finally, we estimate the projected rotation velocity $v \sin i$ between 35 and 40 km s^{-1} as described below.

These results agree on a parameter spectral type of B9Vp rather than B9IIIp as suggested by the *Hipparcos* catalog. Note that it is rather common for spectral types of Ap/Bp stars derived from good classification spectra to select luminosity class III rather than V because the H lines are rather narrow for the lower $T_{\rm eff}$ implicitly assumed (Ap rather than Bp classification) because of the very strong Fe and weak or absent He spectrum. Thus, conventional spectral classification for this star could be of type ApCr (no He lines visible, Fe spectral type later than A0, and strong Cr overabundance are shown below).

3.2 Chemical composition

We need to establish, at least approximately, the abundances of the principal chemical elements that are present in the spectrum, both to more clearly identify what kind of CP star V352 Peg is, and because we need approximate abundances in order to create a suitable line mask to obtain the most precise magnetic measurements possible. There are two main obstacles that prevent a high degree of accuracy in this effort: first, the star is a fairly strong spectrum variable, so (like many magnetic Ap/Bp stars) the abundances of almost all the detectable elements are rather non-uniform over the surface, and therefore the star is not simply characterized by a single abundance value per element; and secondly, the abundances of the main iron group of elements are so large that many weak lines with uncertain atomic parameters crowd the spectrum throughout the visible wavelength window, and make determination of the abundances of less well-represented spectra (such as that of Ti or Pr) rather imprecise.

In fact, we need to obtain two rather different abundance tables. For the precise measurement of magnetic field strengths using the LSD method, our analysis effectively fits the line absorption and polarization profile of each spectral line with a simple model and then averages these fits to obtain a high-S/N measurement of circular polarization. For this purpose, we need an abundance table that leads to a line list that includes lines that approximately reproduce the observed strength of lines when computed with a code that *ignores* the effects of a magnetic field, because the selection process for lines in such line data archives as the Vienna Atomic Line Database (VALD; Piskunov et al. 1995; Pakhomov, Piskunov & Ryabchikova 2017) is carried out ignoring the effects of a magnetic field. For specifying the abundances needed to download a suitable line list, we compute the abundances of the most important elements in the

[1] https://gcpd.physics.muni.cz/

[2] https://vizier.u-strasbg.fr/viz-bin/VizieR-5?-ref=VIZ60e2c396c853e&-out.add=.&-source=I/239/hip_va_1&recno = 2660

Downloaded from https://academic.oup.com/mnras/article/520/3/3201/6651394 by CNRS user on 11 April 2023

Table 1. Summary of observations, taken with the ESPaDOnS spectropolarimeter at the CFHT. The columns indicate the ESPaDOnS odometer number, the observation date, the Heliocentric Julian Date at the middle of the observation (mid-HJD), the observation universal time, the total exposure time in seconds ($T_{\rm exp}$), the S/N, the longitudinal magnetic field (B_l) with its error bars, and the rotation phase of the observations with respect to the reference ephemeris $\rm HJD_0 = 2458348.4725$ and $P_{\rm rot} = 2.63654$ d.

Espadons Odometer number	Date	mid-HJD	UT hh:mm:ss	Exposure (s)	S/N per spec pxl	$B_l \pm \sigma B_l$ (G)	Phase
1331348	2011-08-20	2455793.880	08:46:04	4x410	537	-2486.2 ± 12.5	0.074
2297769	2018-08-18	2458348.876	08:48:41	4x195	158	-2109.9 ± 381.6	0.153
2297797	2018-08-18	2458349.079	13:41:02	4x195	414	-882.4 ± 22.5	0.230
2306359	2018-09-29	2458390.762	06:02:41	4x195	395	-2477.7 ± 15.2	0.040
2306807	2018-10-02	2458393.712	04:49:55	4x195	422	-1864.1 ± 18.7	0.159
2306827	2018-10-02	2458393.931	10:06:29	4x195	416	-654.2 ± 23.2	0.242
2328690	2018-10-18	2458409.888	09:03:27	4x195	448	972.8 ± 22.5	0.294
2329187	2018-10-22	2458413.810	07:12:20	4x195	429	-1461.5 ± 21.2	0.782
2329459	2018-10-23	2458414.814	07:18:42	4x195	458	-1838.1 ± 18.4	0.163
2335338	2018-11-19	2458441.799	06:59:01	4x195	185	2219.0 ± 28.4	0.398
2335342	2018-11-19	2458441.810	07:14:32	4x195	143	2241.2 ± 55.8	0.402
2363446	2018-12-22	2458474.759	06:05:41	4x195	437	-2493.6 ± 13.2	0.899
2363609	2018-12-23	2458475.687	04:21:39	4x195	357	-505.0 ± 22.7	0.251
2363789	2018-12-24	2458476.698	04:37:48	4x195	422	1781.2 ± 17.0	0.634
2363999	2018-12-25	2458477.716	05:03:42	4x195	385	-2462.6 ± 13.1	0.020
2424591	2019-06-08	2458643.120	14:47:43	4x180	416	874.2 ± 20.6	0.756
2425097	2019-06-11	2458646.015	12:15:58	4x180	347	-2377.4 ± 16.3	0.854
2425307	2019-06-12	2458647.074	13:42:09	4x180	396	12.8 ± 21.3	0.256

Table 2. Stellar parameters of V352 Peg. Column 2 indicates the value taken from the reference in Column 3, while Column 4 shows our results.

Parameter	Value	Source	This work
$P_{\rm rot}$ (d)	$2.636\,41 \pm 0.000\,06$	*Hipparcos*	$2.636\,54 \pm 0.000\,08$
$L(L_\odot)$	69.35 ± 11.4	TIC	
$T_{\rm eff}$ (K)	11851 ± 184	TIC	11376 ± 200
$\log(g)$	4.35 ± 0.15	TIC	4.20 ± 0.3
$R(R_\odot)$	1.97 ± 0.1	TIC	
$M(M_\odot)$	3.15 ± 0.1	TIC	
$v \sin i$ (km s^{-1})			35.0 ± 1.5

spectrum assuming zero field strength but a modest microturbulence of 2 km s^{-1}. This set of abundances will be labelled as set 'LL' for 'line list'. In addition, we want to obtain a different set of abundances, ones that approximately represent the average physical abundance ratios in the atmosphere of V352 Peg, which we must compute taking into account the effect of the stellar magnetic field on spectral line formation, and that consider probable abundance variations over the stellar surface in some way. We will call this second set 'MM' for 'magnetic model'.

Abundance fitting for both line lists has been done using the polarized line synthesis program ZEEMAN (Landstreet 1988; Wade et al. 2001; Bailey et al. 2011; Landstreet 2011). The program is built around forwarding computation of the emitted spectrum from an assumed model atmosphere, also assuming an initial abundance table, and if desired a simple model of the stellar magnetic field. The program takes as input a stellar atmosphere interpolated in a grid of ATLAS non-magnetic atmosphere models computed for $T_{\rm eff}$ and $\log g$ values close to those assumed for the star. In its simplest form, the program solves the four coupled equations of transport for polarized radiation propagating through the atmosphere of the specified atmosphere at typically 60 sample points on the visible hemisphere to compute local emergent intensity spectra. These are co-added with appropriate radial velocity shifts (both because of local rotation velocity shifts and due to global radial velocity motion) to predict the observed line spectrum.

This computation uses line lists from VALD, which include both basic atomic data such as $\log gf$ values and damping constants, and also Landé magnetic splitting factors. The abundances assumed in initial requests for the line lists employed in this project all assumed very large overabundances (relative to solar abundances) of even-Z iron peak elements. The equation of transfer is solved outward in the atmosphere at thousands of wavelengths (spaced by 0.01 Å) to predict the emergent spectrum, including at each wavelength the effects of all contributing lines. The program then compares the predicted spectrum with an observed spectrum, and if required, adjusts the abundance table, one element at a time, to find a best-fitting to a chosen spectral window (see e.g. Fig. 1). The stellar radial and rotational velocities are optimized at the same time. We have obtained approximate, but reasonably representative, LL set abundance values by fitting a single spectrum, the spectrum with CFHT odometer number 1331348 from 2011 August 10, which has particularly high *S/N* data. We assumed a microturbulence of $\xi =$ 2 km s^{-1}, and made most of the comparisons in ∼100 Å windows centred at about 4525, 5030, and 6150 Å. In this case, the normal equation of transfer, rather than the polarized version, is solved.

In the case that a magnetic field is present, for the physical abundances table MM, the program employs the appropriate atomic data to include magnetic line splitting (the Zeeman effect), computes at each surface grid point the splitting of all relevant spectral lines, and solves the four coupled equations of transfer for polarized radiation to compute both absorption-line profiles and line polarization (Stokes *Q*, *U*, and *V*). In the present application, the comparison is made only with the absorption-line profiles, again in the same 100 Å wide windows. At each phase, a single local abundance value is assumed, and possible variations of abundance with optical depth are ignored. When possible, the derived abundance values are checked using more than one spectral window. For each of the elements studied, we have modelled our 100-Å windows at three different rotational phases (0.020, 0.254, and 0.398). Because the deduced abundances

Downloaded from https://academic.oup.com/mnras/article/520/3/3201/6651394 by CNRS user on 11 April 2023

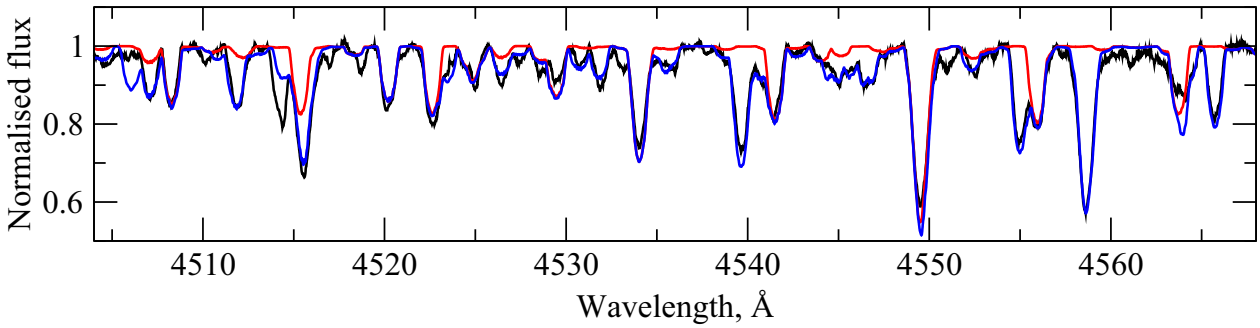


Figure 1. Part of the fit to a spectral window to determine the abundance of Cr. The observed spectrum at phase 0.02 is in black; the fit to the window without Cr is in red, and the best fit to the window after optimizing the abundance of Cr, v_r, and $v \sin i$ is in blue. Spectral features that are sensitive to the abundance of Cr typically have local flux values in the red spectrum near 1.0, but local flux values roughly following the observed spectrum in the blue spectrum.

Table 3. Chemical abundances of V352 Peg. Overabundances and underabundances are computed relative to solar for the MM list.

Element	$\log(\frac{n_X}{n_H})_{LL}$ (dex)	$\log(\frac{n_X}{n_H})_{MM}$ (dex)	Over/under abund. (dex)	Lines (Å)
He	−2.25	−2.5	−1.4	5876
O	−4.35	–	–	7772–5
Mg	−5.0	−5.3	−0.8	4481
Si	−3.75	−4.0	+0.4	5041, 5055–6
Ti	−5.35	−5.9	+1.1	many
Cr	−3.20.	−3.8	+2.5	many
Fe	−2.80	−3.4	+1.1	many
Pr	−7.30	−6.9	+4.4	6160–1 6195
Nd	−7.00	−6.5	+4.0	6145

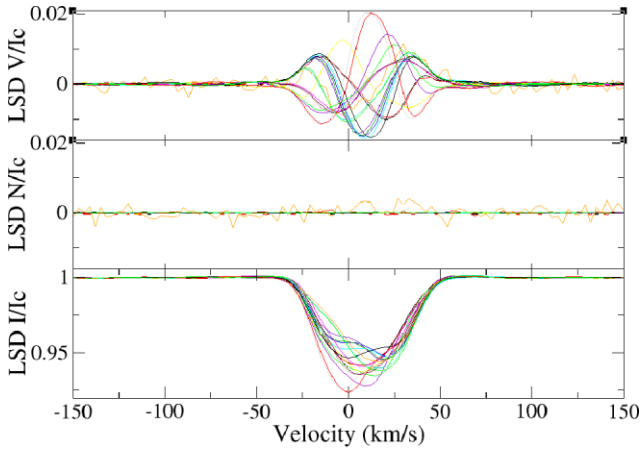


Figure 2. LSD Stokes V (top), Null polarization (middle), and Stokes I (bottom) profiles obtained after the LSD of the 18 ESPaDOnS spectra.

from two or three windows at a single-phase generally differ by an amount of order 0.2 dex, and similar differences occur from one phase to another, we report a representative compromise abundance for the elements studied. For other elements (O, Mg, Si, Pr, and Nd), only one or a few suitable lines are available in the spectrum, but we have again considered three phases. Realistically all of this abundance should be regarded as uncertain by an amount of order 0.2–0.3 dex.

The resulting abundance values of elements X relative to H, $\epsilon = \log(n_X/n_H)$, are tabulated in Table 3. The second column lists table LL, and the third column table MM. We also list the enhancement or deficiency (in dex) of abundance set MM relative to the solar abundance table as reported by Asplund et al. (2009). When a very small number of spectral lines are fit to obtain the abundance, the lines used are noted (by wavelength in Å units) in Table 3. The rare earths Pr and Nd are rather marginally detected in the spectra. Note that no physical abundance is provided for the element O, as the best lines for modelling exhibit very large non local thermodynamic equilibrium effects that we are unable to correct.

The dominant peculiarities of this star are the underabundances of He, O, and Mg, and the large overabundances of the iron peak elements Ti, Fe, and especially Cr. However, such abundance anomalies are not unusual for magnetic Ap stars: compare, for example, with the abundance tables found by Bailey et al. (2011) and Bailey & Landstreet (2013) for the slightly hotter magnetic Ap stars HD 318107 and HD 147010.

4 SPECTROPOLARIMETRIC ANALYSIS

4.1 Stokes I and V profiles

A least-square deconvolution (LSD) is applied to the data, based on the method described in Donati (1997). The LSD algorithm requires, as an input, a line mask listing the lines present in the spectra. A template mask was first extracted from VALD3 for $T_{\rm eff} = 11\,500$ K and $\log g = 4.0$ and using the chemical abundances determined above. We used only lines with a depth larger than 1 per cent of the continuum. We cleaned the mask of hydrogen lines and lines blended with either hydrogen or telluric lines. The final mask contains 5010 lines. We then adjusted the depth of each line in the mask to the observed line depth. Due to strong-line variation between the different spectra, we chose to use a mask with tailored depths per spectrum to obtain more accurate values of the magnetic field. This choice will be discussed in Section 5.

The circularly polarized spectrum can be written as a convolution of the mean Zeeman signature and the line pattern (see equations presented in Donati (1997) and Kochukhov, Makaganiuk & Piskunov (2010) for more details). Polarization information is simultaneously extracted from all the spectral lines present in the mask.

The Stokes V and I profiles and Null polarization of V352 Peg are plotted in Fig. 2. Zeeman signatures are visible in all the Stokes V spectra, with an amplitude up to 2 per cent, while N profiles appear

Downloaded from https://academic.oup.com/mnras/article/520/3/3201/6651394 by CNRS user on 11 April 2023

featureless. The Stokes V measurements show variable profiles, typical of a rotational modulation of the magnetic signature. The typical inverse error on Stokes V profiles is 10 800. The Stokes I profiles also show variability, typical of the presence of chemical spots at the surface of the star.

After the deconvolution, the False Alarm Probability (FAP) is computed from the Stokes V and N profiles. This statistical quantity is a detection probability based on the χ^2 statistics. It is determined both inside and outside the stellar lines and characterizes the presence of a Zeeman signature in the Stokes V profile, enabling to distinguish between a real signature and noise. A detection is classified as definite if the FAP is smaller than 10^{-5}, corresponding to a detection probability of 99.999 per cent. The signature is marginally detected if the FAP falls in the interval [10^{-5}, 10^{-3}] and is not detected for a FAP greater than 10^{-3}.

Inside the stellar lines, the presence of a magnetic field is definitely detected for the 18 observations. There is also a definite detection for 16 observations outside the stellar lines, due to undulations in the continuum, greater than the noise level. This could be due to small imperfections or errors during the LSD process. An other probable explanation is the residual effects of nearby lines. The two observations with no detection outside the line profile are the ones with the lowest S/N (observations #2 and #11), thus with the higher noise level hiding the undulations.

There is no detection in the N profiles (see Fig. 2).

4.2 Longitudinal magnetic field

The longitudinal magnetic field B_l can be computed from the Stokes V and I profiles (Donati 1997), with the following formula:

$$B_l = -2.14 \times 10^{11} \frac{\int v V(v) \mathrm{d}v}{\lambda g c \int [I_c - I(v) \mathrm{d}v]} \quad (1)$$

where λ and g are the scaling wavelength and Landé factor of the stellar lines used to obtain the LSD profile. We used the mean wavelength $\lambda = 5406$ Å and the mean Landé factor $g = 1.19$ to scale the LSD profiles.

The value of B_l varies with the rotation of the star. This is due to a misalignment between the rotation and the magnetic axes, postulated by the Oblique Rotator Model (Stibbs 1950). For a dipole field, when the stellar magnetic axis is seen 'pole-on' (pointing in the direction of the observer), the longitudinal magnetic field is at an extremum. On the other hand, when we observe the stellar magnetic equator, B_l is 0 G.

The values of the longitudinal magnetic field for V352 Peg are presented in Fig. 3. The data being of very high-quality, only one error bar, corresponding to the noisiest spectrum (#2) is visible. The black and blue-dotted lines in Fig. 3 represent fits to the data described respectively by equations (2) and (3):

$$B_l(x) = a + b \times \sin(x + c) \quad (2)$$

$$B_l(x) = a + b \times \sin(x + c) + d \times \sin(2x + e) \quad (3)$$

Parameters of the fit are given in Table 4. The errors have been computed from the error on B_l.

The variation of the longitudinal magnetic field is better fit with a sine wave described by equation (3) rather than by equation (2). The minimum and maximum values of the dipolar fit to the longitudinal magnetic field values are: $B_{\mathrm{l,\,min}} = -2920 \pm 15$ G and $B_{\mathrm{l,\,max}} = 2370 \pm 15$ G.

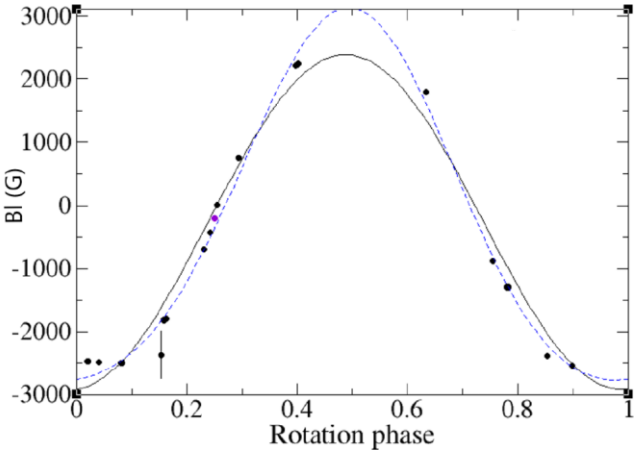


Figure 3. Longitudinal magnetic field of V352 Peg, folded in phase with $\mathrm{HJD_0} = 2458348.4725$ and $\mathrm{P} = 2.63654$ d. The solid black and dotted blue lines are a single-wave and a double-wave fits to the data as defined in equations (2) and (3).

Table 4. Parameters of the single-wave and double-wave fits to the longitudinal magnetic field values.

Single-wave	Double-wave
$a = -274.23 \pm 5.75$	$a = -179.02 \pm 0.30$
$b = 2645.49 \pm 8.26$	$b = 2943.47 \pm 0.48$
$c = -0.2385 \pm 0.0004$	$c = -0.2395 \pm 2 \times 10^{-5}$
-	$d = 350.07 \pm 0.38$
-	$e = 0.2468 \pm 9 \times 10^{-5}$
Reduced $\chi^2 = 256$	Reduced $\chi^2 = 90$

4.3 Rotation period determination from magnetic field measurements

The variation of the longitudinal magnetic field with time can be used to refine the rotation period.

The observations available are unevenly spaced in time. Instead of the Fourier transform, a more suitable way to find the rotation period is a least-squares spectral analysis. This method estimates the frequency spectrum based on a least-squares fit of sinusoids to the data set. Our data set contains only a small number of data points. Thus, a generalized Lomb–Scargle periodogram (GLS; Zechmeister 2009) is used to find the peak frequency of the signal. Fig. 4 has been computed based on a PYTHON implementation of the GLS developed by Jake VanderPlas and reported by Željko Ivezic Connolly et al. (2014).

The two dotted lines represent the significance levels at 1 per cent and 10 per cent. Two peaks exceed this threshold: 1.52 and 2.636 05 d. The peak at 2.63605 d is detected with a power of 0.97 and is coherent with the rotation period of 2.64 d presented in the *Hipparcos* catalog (ESA 1997). We have no physical explanation for the peak at 1.52 d, but Fig. 4 seems to show a group of incoherent peaks around 1.4–1.5 d so that the 1.52 d value should probably not be considered as a single exact peak. The longitudinal magnetic field for the rotation period found using the GLS is plotted in Fig. A1. The fit seems to be in good agreement with the data points. However, by plotting the Stokes I and V profiles (see Section 4.5), we detected a small error on the rotation period: while the observations from 2011 August 19 and 2018 December 21 have

Downloaded from https://academic.oup.com/mnras/article/520/3/3201/6651394 by CNRS user on 11 April 2023

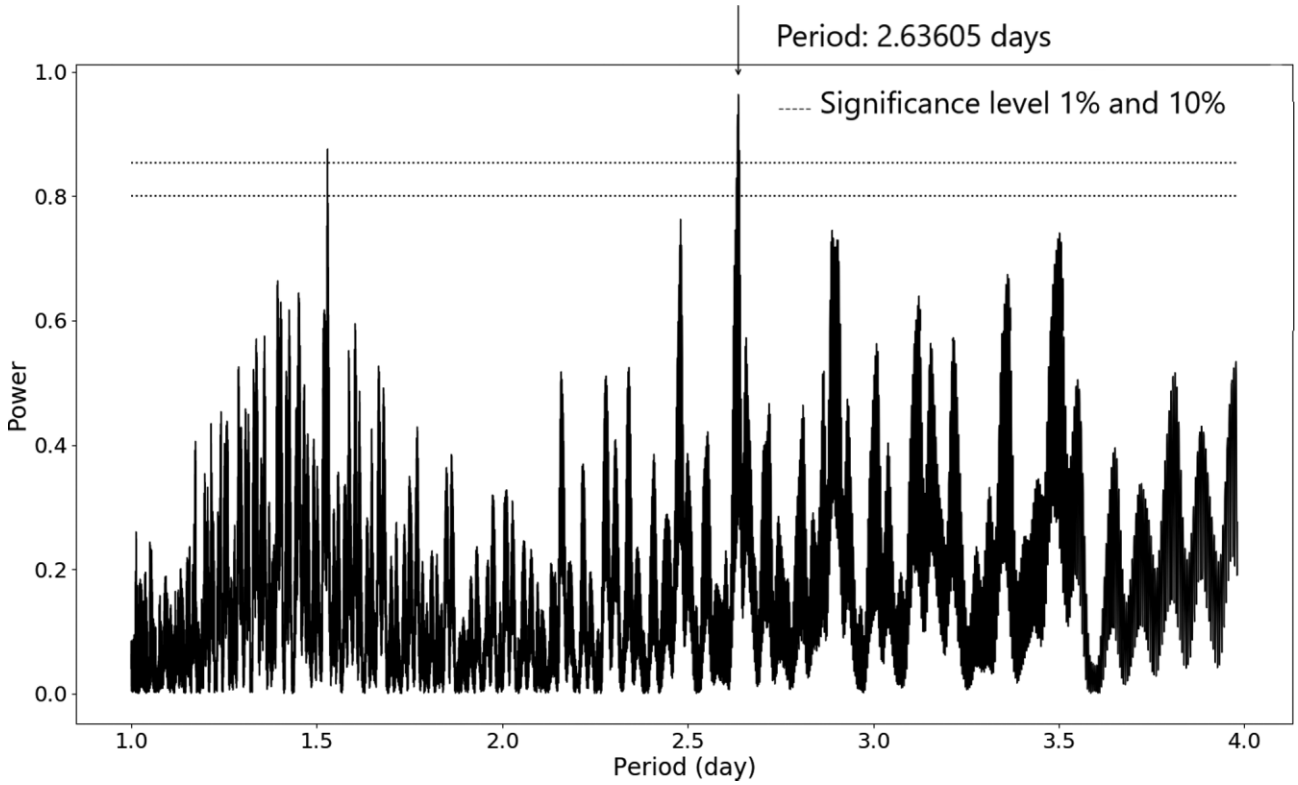


Figure 4. GLS periodogram of V352 Peg. The two horizontal dotted lines represent the 1 per cent and 10 per cent significance levels.

a small difference in phase visible in Fig. A2, they have different magnetic signatures. Thus, we used the following reasoning to refine the rotation period.

Between the first observation on 2011 August 19 and the mid-day of all other observations, the star rotated $N = 1012$ times. Thus, a small error on the rotation period will have a strong impact on the phase of the 2011 MiMeS data point. Such an error can be estimated based on the misfit between the phase of this point and the expected phase from the dipolar fit. The expected period phase of V352 Peg, ϕ_{exp}, when the 2011 observation was recorded, can be calculated from the dipole magnetic field model given by equation (2). It is estimated to be $\phi_{exp} = 0.08968$. The MiMeS point phase found with the rotation period of 2.63605 d is $\phi_{obs} = 0.90131$. It represents a difference in phase of $\Delta\phi = 1 - \phi_{obs} + \phi_{exp}$, thus an error on the rotation period of $e = \frac{P \times \Delta\phi}{N} = 4.9 \times 10^{-4}$, where $P = 2.63605$ d. The final period we determined is $P_{\rm rot} = 2.63654 \pm 0.00008$ d. In the following, all the observations of V352 Peg are thus phased according to this period and the following reference date $\mathrm{HJD}_0 = 2458348.4725$.

4.4 Dipolar configuration derived from the magnetic field measurements

We model the magnetic field of V352 Peg as a dipole and use the Oblique Rotator Model, first introduced in Stibbs (1950). Four parameters are required to describe this model: the inclination angle i between the rotation axis of the star and the line of sight, the obliquity angle β between the rotation and the magnetic axes, the rotation period $P_{\rm rot}$, and the surface polar field strength of the magnetic dipole $B_{\rm dip}$.

The inclination angle can be constrained from the rotation period and the stellar radius R:

$$\sin i = \frac{v \sin i \, P_{\rm rot}}{2\pi R} \tag{4}$$

From this equation, the inclination angle is estimated to be $i = 66.4 \pm 5.4^\circ$.

The ratio between the minimum and maximum longitudinal magnetic field strength is directly linked to the angles i and β (Preston 1967):

$$r \equiv \frac{B_{\rm l,min}}{B_{\rm l,max}} = \frac{\cos(i+\beta)}{\cos(i-\beta)} \tag{5}$$

Using the values specified in Section 4.2, the ratio is estimated to be $r = -1.23 \pm 0.01$. With this ratio and the inclination angle determined above, the obliquity angle is: $\beta = 103.3 \pm 7.2^\circ$.

Finally, $B_{\rm dip}$ can be estimated from the relation (Schwarzschild 1950):

$$B_{\rm l,max} = \frac{15+u}{15-5u}\frac{B_{\rm dip}}{4}\cos(i-\beta), \tag{6}$$

where u, the limb-darkening coefficient, is taken equal to 0.4445, according to Claret (2019). We thus obtain a polar magnetic field strength, assuming the field is dipolar, $B_{\rm dip} = 9635 \pm 1150$ G.

The limb-darkening coefficient has been selected from table 6 of Claret (2019), using $T_{\rm eff} = 11\,500$ K, $\log g = 4$, and a microturbulent velocity of 4 km s^{-1}. The mean wavelength of the blue passband of Gaia mission being 516.47 nm, close to the mean wavelength of the observations (541.08 nm), we used u1 coefficient from Claret's table 6 computed using the ATLAS stellar atmosphere model and the least-square method at the Gaia blue wavelength.

Downloaded from https://academic.oup.com/mnras/article/520/3/3201/6651394 by CNRS user on 11 April 2023

4.5 Mapping the surface magnetic field and relative-line strengths

4.5.1 Zeeman–Doppler Imaging model description

Methods to map the chemical spots of Ap/Bp stars were developed in the 70's, based on line intensity variations in the spectra of magnetic CP stars. (Khokhlova 1976; Goncharskii et al. 1982). Based on the same principles, Vogt & Penrod (1983) introduced the Doppler Imaging method, enabling to obtain a resolved image of a star with temperature spots from spectral line profile distortions. The ZDI method was introduced in the 80s (Piskunov & Khokhlova 1983, 1984; Semel 1989). It relies on a similar idea as the Doppler Imaging (DI) technique but applied to circularly polarized data. DI uses the Doppler effect, applied to rotationally broadened spectral lines, and achieves spatial resolution by mapping the wavelength position along a spectral line to the spatial position across the stellar disc. An inhomogeneous surface-brightness affects the shape of the spectral lines. A darker area produces a bump in the intensity line while a brighter spot generates a depression. The position of this deformation is modulated by the rotation of the star: as the star rotates, the darker or brighter region propagates across the visible hemisphere of the star and the associated bump or depression propagates across the line profile. Similarly, a difference in the magnetic field across the stellar surface affects the shape of the spectral lines in total intensity and polarization. Through a modelling of Stokes I and V profiles, ZDI aims at reconstructing the vectorial magnetic field at the stellar surface.

ZDI can be performed using individual lines (Silvester, Kochukhov & Wade 2014) and LSD profiles (Kochukhov et al. 2014, 2017). An alternative method to reconstruct the surface magnetic field of hot stars is the use of parametrized magnetic field and chemical spots models (Bailey et al. 2012; Bailey & Landstreet 2013). Linear polarization data (Stokes Q and U) can be added, enabling to recover more complex field typologies and detailed magnetic field maps (Silvester et al. 2014).

Reconstructing a brightness or magnetic map based on a set of line profiles is an ill-posed inverse problem with multiple acceptable solutions. To solve this, one needs an additional regularization constraint, we use the maximum entropy method (Skilling & Bryan 1984).

The magnetic field topology can be decomposed in spherical harmonics, according to the following set of equations (Donati et al. 2006):

$$B_r(\theta,\phi) = \sum_{l=0}^{l_{max}} \sum_{m=0}^{l_{max}} \alpha_{l,m} Y_{l,m}(\theta,\phi) \tag{7}$$

$$B_\theta(\theta,\phi) = -\sum_{l=0}^{l_{max}} \sum_{m=0}^{l_{max}} \beta_{l,m} Z_{l,m}(\theta,\phi) + \gamma_{l,m} X_{l,m}(\theta,\phi) \tag{8}$$

$$B_\phi(\theta,\phi) = -\sum_{l=0}^{l_{max}} \sum_{m=0}^{l_{max}} \beta_{l,m} X_{l,m}(\theta,\phi) - \gamma_{l,m} Z_{l,m}(\theta,\phi) \tag{9}$$

where θ and ϕ are the colatitude and longitude at the stellar surface. $X_{l,m}$, $Y_{l,m}$, and $Z_{l,m}$ are the spherical harmonic modes and their derivatives, depending on the Legendre polynomial. The parameters, $\alpha_{l,m}$ and $\beta_{l,m}$, characterize the poloidal component of the magnetic field and $\gamma_{l,m}$ the toroidal part. The summation is carried out over positive spherical harmonic order m, and over degree l varying from 0 to l_{max}. The choice of l_{max} is discussed in Appendix D.

The stellar surface is modelled by a grid of equal area surface elements. From the above spherical harmonic coefficients, the magnetic field at the element j is evaluated to obtain the vector $[B_r(\theta_j, \phi_j), B_\theta(\theta_j, \phi_j), B_\phi(\theta_j, \phi_j)]$. Based on that vector and the local line strength b_j, the local line profile $\mathbf{F}_j = (I_j, V_j)$, gathering the two local Stokes parameters, is calculated. Finally, using the set of $\mathbf{F}_j$ and integrating over the surface of the star, one can get the final line profile $\mathbf{F} = (I, V)$. Thus, by knowing $\alpha_{l,m}$, $\beta_{l,m}$, $\gamma_{l,m}$, and b_j, and given a line profile model, one can calculate the local line profiles F_j and then obtain the desired disc integrated Stokes spectra: this is the forward problem. The inverse problem consists of reconstructing a magnetic configuration and brightness spots, based on an observed time series of Stokes I and V spectra. This is solved by iteratively fitting a model Stokes I and V profiles to the observations to minimize the χ^2, subject to the additional regularization constraint of maximizing entropy in the brightness and magnetic field distributions.

The code used to perform the mapping is based on Folsom et al. (2018). This is a PYTHON implementation of the code presented by Donati et al. (2006) and uses the maximum entropy method of Skilling & Bryan (1984), which both minimizes the χ^2 and maximizes the entropy to obtain a unique solution. We have made one major modification to the code of Folsom et al. (2018). In Ap stars, the Stokes I variability is pre-dominantly driven by chemical spots, which produce variations in line strength, while the DI of Folsom et al. (2018) was based on mapping brightness variations due to temperature spots. These effects have some similarities, but brightness variations do not change the equivalent width of a line while chemical spots do. Thus we have modified the code to map relative-line strength, as a proxy for chemical abundance, instead of relative brightness. The implementation of this modification is relatively straightforward. The local Stokes I line profile becomes:

$$I_j(\lambda) = a_j d_j (1 - b_j u(\lambda)) \tag{10}$$

for a local line strength b_j, using a Voigt function u for wavelength λ, with a limb darkening d_j, and projected surface area a_j, for surface element j. Then the disc integrated, continuum normalized profile is:

$$I(\lambda)/I_c = \frac{\sum_j I_j(\lambda)}{\sum_j a_j d_j} \tag{11}$$

where j is summed over visible surface elements. The Stokes V local line profile is calculated using the weak field approximation (WFA) and incorporates the distribution of local line strengths. That becomes:

$$V_j(\lambda) = -g_{\rm eff}\lambda_0^2 c_0 B_{l,j} \frac{{\rm d}I_j(\lambda)}{{\rm d}\lambda} = g_{\rm eff}\lambda_0^2 c_0 a_j d_j b_j B_{l,j} \frac{{\rm d}u(\lambda)}{{\rm d}\lambda} \tag{12}$$

where $B_{l,j}$ is the line-of-sight component of the magnetic field for surface element j, $g_{\rm eff}$, and λ_0 are the effective Landé factor and wavelength of the line (or the normalizing values for an LSD profile), and the constant $c_0 = \frac{e}{4\pi m c^2}$ using the electron charge e, mass m, and speed of light c. Then the disc-integrated continuum normalized Stokes V profile is:

$$V(\lambda)/I_c = \frac{\sum_j V_j(\lambda)}{\sum_j a_j d_j}. \tag{13}$$

This provides a model that incorporates the variation in line strength (equivalent width) produced by chemical abundances spots for both Stokes I and V. We caution that there is not a linear mapping between the relative-line strength mapped here and specific surface abundance values, since line equivalent width depends non-linearly on abundance. However, areas of relatively higher or lower line strength do correspond to areas of higher or lower chemical abundance.

Downloaded from https://academic.oup.com/mnras/article/520/3/3201/6651394 by CNRS user on 11 April 2023

The local line profile model is a Voigt profile, a convolution of a Gaussian and a Lorentzian profile. Theoretically, this provides the combination of thermal and turbulent broadening with natural and collisional broadening. Practically, a simple Gaussian is often insufficient to accurately reproduce the Stokes I line shape at high resolution, and since such errors could lead to artefacts in a map, a Voigt profile is preferable. The Gaussian width was set to 5.9 km s^{-1} to account for the thermal and turbulent broadening and the Lorentzian width to 0.6 km s^{-1}. The local Lorentzian and Gaussian widths both have relatively large uncertainty. They are also potentially influenced by strong systematic effects such as Zeeman broadening and imperfections in the LSD process, so the values should be treated with caution if interpreting them physically. However, realistic uncertainties on these parameters have a small impact on the derived maps, mostly just changing the contrast of small-scale features. We find that taking the Gaussian width in the interval [4 km s^{-1}, 7 km s^{-1}] and the Lorentzian width in [0 km s^{-1}, 2 km s^{-1}] yields to approximately the same results, with a slightly better χ^2 reached for the adopted set of widths. The instrumental broadening is accounted for after the disc integration by convolving the disc-integrated line profile with a Gaussian instrumental profile with R = 65 000, as described in Folsom et al. (2018). The scaling wavelength and Landé factor have been taken equal to the mean values from the LSD calculation, i.e. $\lambda = 540.6$ nm and $g = 1.19$. The parameter controlling the entropy slope, the effect of which is explained in Appendix C, is taken equal to 200. The highest spherical harmonic degree $l_{\max}$ used to compute the magnetic field is 10. These two parameters have been chosen accordingly to tests presented in Appendices C and D.

Two statistical tests are used to assess the quality of the ZDI solution. First, the χ^2 statistics attests of the goodness of the fit, i.e. whether the simulated Stokes I and V profiles match the observed one. An ideal fit has a reduced $\chi^2 = 1$. In this study, we used the approximation that the reduced χ^2 is equal to the χ^2 divided by the total number of observed points. The second test is introduced in Skilling & Bryan (1984):

$$\mathrm{TEST} = \frac{1}{2}\left|\frac{\nabla S}{|\nabla S|} - \frac{\nabla C}{|\nabla C|}\right|^2 \tag{14}$$

TEST measures how antiparallel the gradients in entropy and χ^2 are. The entropy used is defined in Folsom et al. (2018) by equations (B11) and (B13), introduced respectively in Hobson & Lasenby (1998) for the magnetic spherical harmonic coefficients and Skilling & Bryan (1984) for the relative-line strengths. A fully converged image should have TEST = 0. Thus, the suitable magnetic and line strength configuration should ideally have $\chi^2 = 1$ and TEST = 0.

4.5.2 *Refinement of the stellar parameters with ZDI*

The inclination i and the projected rotation velocity can be refined using ZDI, based on the method presented in Petit, Donati & Collier Cameron (2002). A grid of inclination angles and $v\sin i$ values is generated. A target entropy is set while χ^2 remains unconstrained. For each value of the inclination angle, the ZDI algorithm is run to fit the observed Stokes V profiles. The result of this method is presented in Fig. 5. The same method is used to refine the projected rotation velocity but Stokes I profiles are used instead of V in this case, because Stokes V is much less sensitive to $v\sin i$ than Stokes I (and conversely for the inclination). The optimal parameter is the one minimizing χ^2 for a given target entropy. Another procedure yielding approximately the same result consists in setting a target χ^2 value and a free entropy. The optimal parameter is then the one maximizing the entropy for a fixed χ^2.

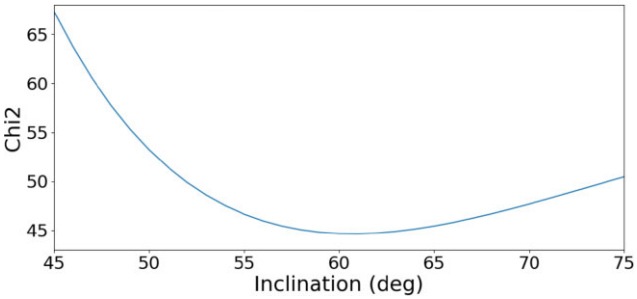


Figure 5. Refinement of the value of the inclination angle i with a target entropy $E = -180\,000$.

Folsom et al. (2018) described a method to compute the error on the parameters based on the significance of variations in the χ^2 statistic. The variation in the χ^2 about the minimum corresponding to a 1σ confidence level provides the range of the reported error in i (or $v\sin i$). After computation of the error, the inclination is set to $i = 62^{\circ}{}^{+9}_{-7}$, agreeing with the value of $i = 66.4^{\circ} \pm 5.4$ derived from the longitudinal field curve and presented in Section 4.4, within error bars. The same procedure is used to refine the projected rotation velocity. A value of $v\sin i = 35.0 \pm 1.5$ km s^{-1} is adopted. We note that Zeeman splitting is not explicitly included in the Stokes I line model, this could lead to an overestimate of vsini, or of the local line width, and both parameters may be overestimated by a few km s^{-1}.

4.5.3 *Magnetic and relative-line strength configuration of V352 Peg*

The results of the fit to Stokes I and V profiles using the optimized stellar parameters are plotted in Fig. 6. The goodness of the fit is assessed by the χ^2 value and TEST parameter. Stokes I profiles were fitted to a reduced χ^2 of 100 while the final reduced χ^2 from Stokes V fit is 40. These values might appear high, the optimal value being 1. This can be explained because the error bars on the Stokes I and V LSD profiles are extremely small.

2D surface reconstruction of V352 Peg for five different rotation phases are plotted in Fig. 7. The magnetic equator is visible, almost aligned with the rotation axis. The obliquity angle between the magnetic and rotation axes is estimated to be $\beta = 91.5 \pm 7.0^{\circ}$. Like the inclination angle, the obliquity angle estimated with ZDI agrees with the estimate (see Section 4.4) of $\beta = 103.3 \pm 7.2^{\circ}$ derived from the longitudinal field curve, within the error bars. The polar magnetic field strength is $B_{\mathrm{dip}} = 6320^{+170}_{-280}$ G, differing more from the analytical estimate. This difference is discussed in Section 5. Both B_{dip} and β have been estimated from the radial poloidal $l = 1$ component of the magnetic field using ZDI. The error on these two parameters has been computed by propagating the error on i in equations (5) and (6).

From Figs 7 and 8, the magnetic field is clearly dipolar. However, there is a clear asymmetry in the strength of the magnetic field between the positive and negative regions. The magnetic field strength reaches 5200 G in the positive hemisphere while its maximum in the magnetic negative hemisphere is 4900 G (in absolute value). Moreover, the magnetic field strength is not homogeneous within a magnetic hemisphere, as attested by spots of stronger magnetic field visible in the radial magnetic field map in Fig. 8.

Downloaded from https://academic.oup.com/mnras/article/520/3/3201/6651394 by CNRS user on 11 April 2023

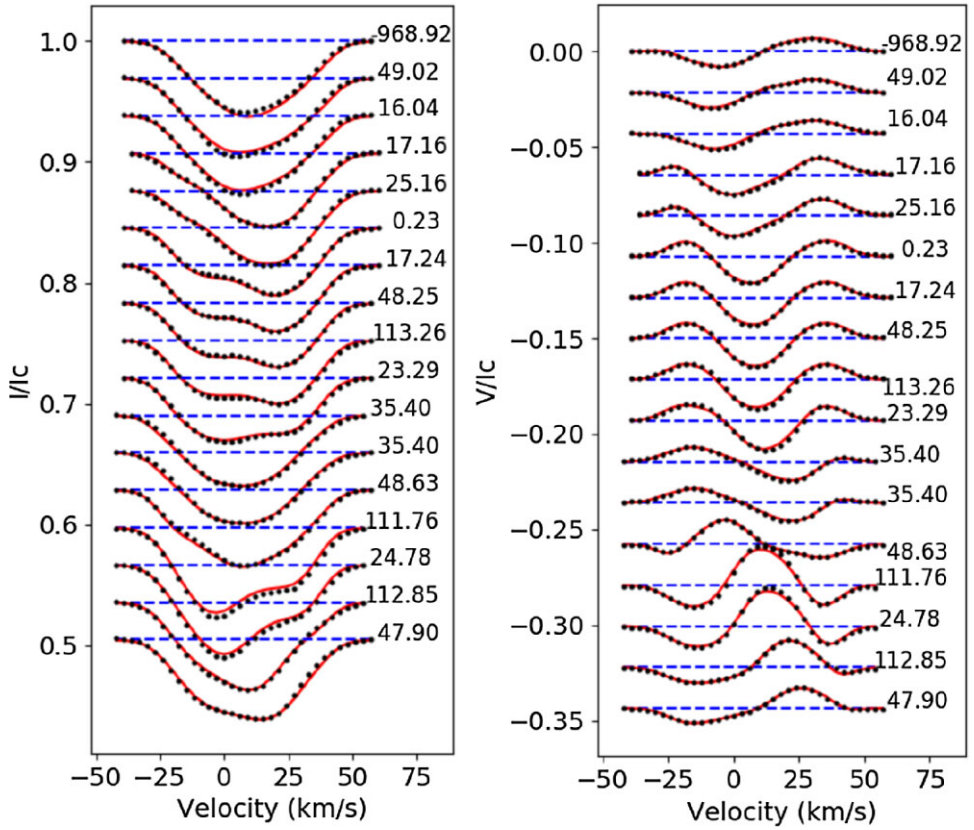


Figure 6. Comparison between observed (black dots) and simulated (red lines) Stokes I (left-hand panel) and V (right-hand panel) profiles. The profiles are shifted vertically according to their rotation phase, which is indicated next to each profile.

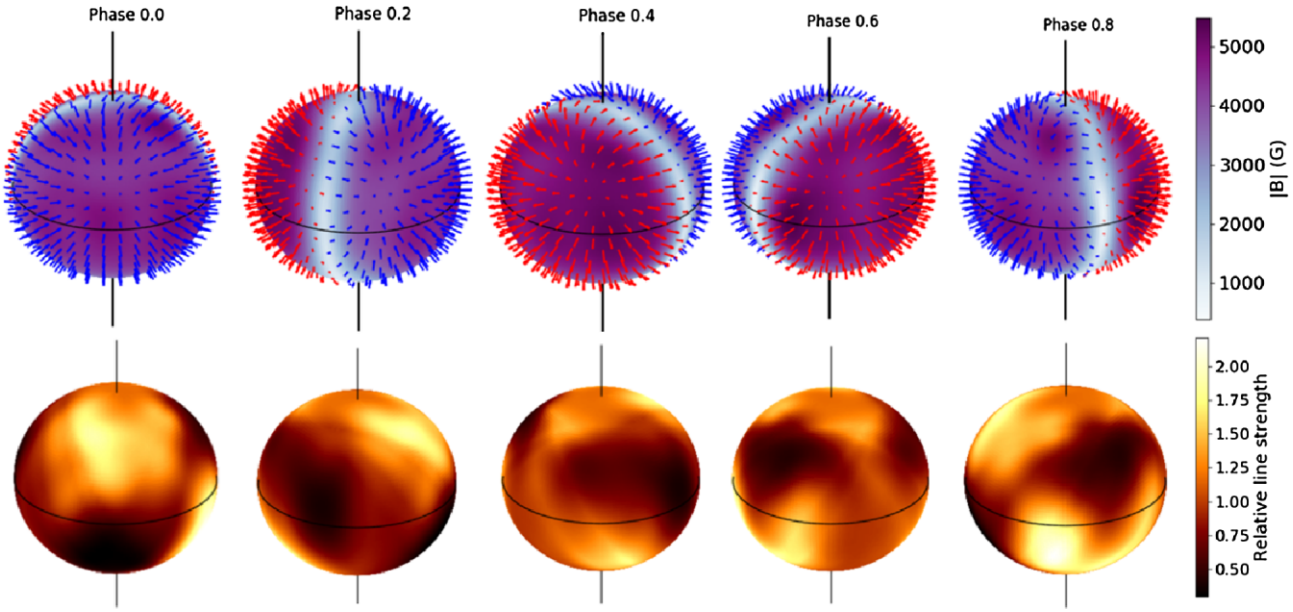


Figure 7. Magnetic (top row) and relative-line strength (bottom row) maps of V352 Peg. Each column corresponds to a different rotation phase. The black axis is the rotation axis. The colours represent the magnetic field strength in Gauss (top row) and the relative-line strength (bottom row). The arrows at the stellar surface indicate the vectorial magnetic field (red arrows have a positive radial field and blue arrows have a negative radial field).

Downloaded from https://academic.oup.com/mnras/article/520/3/3201/6651394 by CNRS user on 11 April 2023

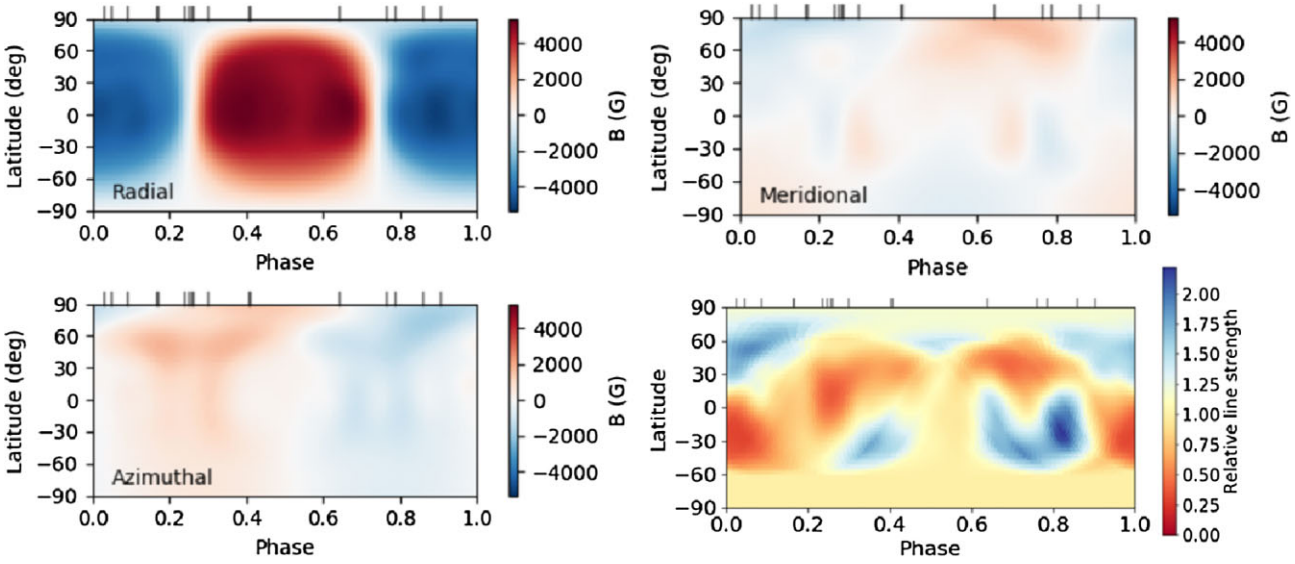


Figure 8. ZDI map for V352 Peg. The vertical lines above each map indicate the phases of individual spectra. The figure on the bottom-right represents the relative-line strength.

Table 5. Magnetic field energies obtained through ZDI.

Magnetic component	Percentage
Poloidal	98.5 per cent (per cent tot)
Toroidal	1.5 per cent (per cent tot)
Axisymmetric	0.4 per cent (per cent tot)
Dipole	91.1 per cent (per cent pol)
Quadrupole	1.0 per cent (per cent pol)
Octopole	5.9 (per cent pol)
Poloidal axisymmetric	0.31 per cent (per cent pol)
Toroidal $l = 1$	31.9 per cent (per cent tor)
Toroidal $l = 2$	18.1 per cent (per cent tor)
Toroidal $l = 3$	7.7 per cent (per cent tor)
Toroidal axisymmetric	7.0 per cent (per cent tor)
Dipole axisymmetric	0.1 per cent (per cent dip)

The relative-line strength map is shown in the bottom row of Fig. 7. Two large spots of high relative-line strength are visible at $\phi = 0$ in the Northern hemisphere and at $\phi = 0.8$ in the Southern hemisphere. In addition, the magnetic equator, observable at the rotation phases 0.2, 0.4, 0.6, and 0.8, seems to coincide with regions of lower relative-line strength (thus lower absorption), except in the polar regions. The relative-line strength configuration does not exactly follow the dipole configuration of the magnetic field. This is also visible in the polar projection maps in Fig. 8.

The magnetic field energies in different components of the geometry are described in Table 5 and taken to be proportional to B^2. An other way of seeing the configuration is by plotting the modulus of the spherical harmonic coefficients. This is done in Fig. 9. The axisymmetric modes correspond to $m = 0$ spherical harmonics.

The magnetic field is mainly poloidal, with a very weak toroidal component contributing to only 1.5 per cent of the total magnetic energy. The poloidal field is dominantly dipolar (91.1 per cent) and non-axisymmetric, with weak contributions from the quadrupolar and octupolar components. For the coefficients $\alpha_{l,m}$ and $\beta_{l,m}$, the dominant mode is $l = 1$ and $m = 1$, corresponding to a non-axisymmetric dipole. Contrary to the poloidal field, the toroidal part is characterized by a stronger contribution from higher-order multipoles (essentially quadrupole and octupole with $m = 1$ and $l = 2, 3$). However, since the toroidal component is very weak, it is not clear how reliable the geometry is. Modes with $l > 6$ contribute faintly to the image reconstruction, so do axisymmetric modes ($m = 0$), especially for the poloidal part of the magnetic field.

4.5.4 Surface distribution of Titanium, Chromium, and Iron

Surface distribution maps can be obtained for Titanium, Chromium, and Iron (elements with a high number of spectral lines, see Table 3).

The surface distribution of an element can be inferred from the variation of local line strength (or local equivalent width; Hatzes, Penrod & Vogt 1989; Hatzes 1991). A region enhanced in a chemical element will create deeper absorption features in the spectra, increasing the local equivalent width (proportional to the local line strength). Thus, by modelling the local line strength variation, we can obtain information about the surface distribution of chemical elements.

As mentioned in Hatzes et al. (1989), going from a local equivalent width to actual abundances is not trivial. In this section, we aim at approximating the surface distribution of an element in terms of stronger or weaker local line strength, which should correlate with enhanced or depleted abundances.

Spectral lines from Cr, Fe, and Ti are used to reconstruct the surface distribution of these elements. To this aim, LSD profiles are produced from a subset of lines extracted from the original LSD line mask (see Section 4.1). We used around 2000 lines of Cr, 3000 lines of Fe, and 190 lines of Ti.

Results are presented in Fig. 10. The surface distribution of Cr, Fe, and Ti is inhomogeneous. As expected from the clear variations observed in the line profiles, chemical spots are present at the surface of V352 Peg. The Stokes I and V profiles are very well-fitted for

Downloaded from https://academic.oup.com/mnras/article/520/3/3201/6651394 by CNRS user on 11 April 2023

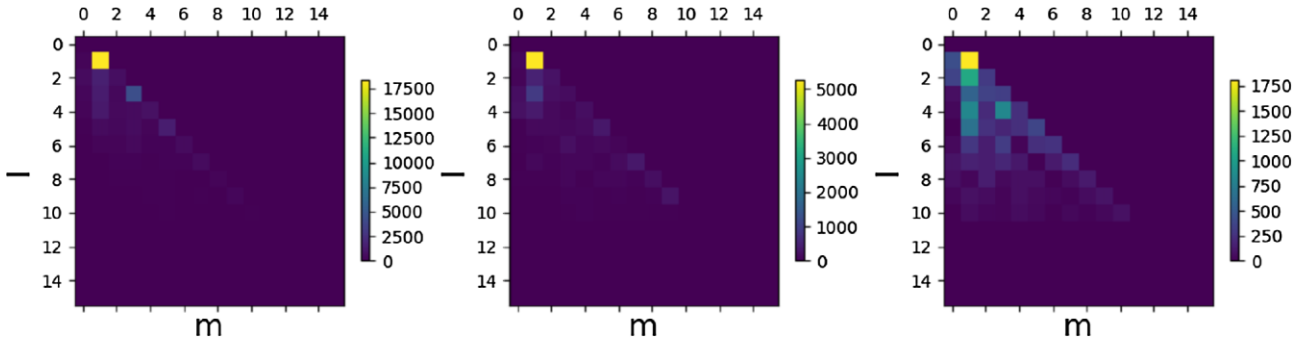


Figure 9. Modulus of the spherical harmonic complex coefficients as a function of mode degree l and order m. $\alpha_{l,m}$, $\beta_{l,m}$, and $\gamma_{l,m}$ correspond respectively to the radial field component, tangential component of potential field term, and tangential component of toroidal field term.

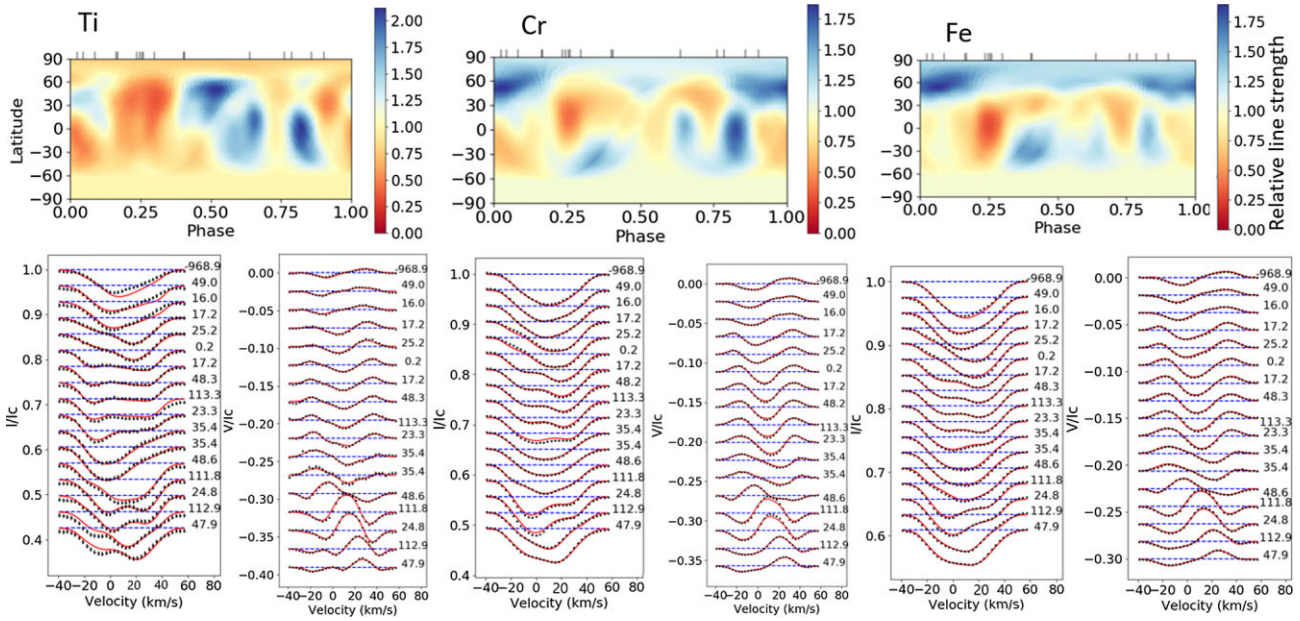


Figure 10. Relative-line strength map of Ti, Cr, and Fe. The corresponding fit to Stokes I and V profiles is shown below each map.

Iron and Chromium. For Titanium, the ZDI code struggles to fit the profiles at phases 112.85, 47.90 and −968.92. These phases should coincide with the Southern magnetic hemisphere entering in the line of sight, around phase 0.9 in the map from Fig. 10. By comparing Figs 8 and 10, one can see that Ti seems to gather around the magnetic equator, visible at the phase 0.75 in Fig. 8. The distribution of Cr and Fe is very similar and more complicated to link to the magnetic topology. There is an overabundant region located in the Northern polar region. The overall distribution of these two chemical elements could be linked to the meridional magnetic field map in Fig. 8 but there is no clear trend.

5 DISCUSSION

In this study, we have used the LSD method, which assumes that the magnetic field is weak and that the lines considered in the line deconvolution have a similar profile. The WFA might be a questionable assumption as the polar magnetic field strength we derived in the ZDI model reaches $B_{\rm dip} = 9.6$ kG. Landi Degl'Innocenti & Landolfi (2004) suggested that the weak field regime breaks down around 1 kG for iron-peak spectral lines. In addition, Kochukhov et al. (2010) showed that the LSD single line approximation becomes inaccurate with increasing magnetic field strength. Using the WFA also has an impact on the modelling with ZDI. Thus, we designed a test to check for the validity of the WFA.

We calculated line profiles for a dipole magnetic field with strength of 500 G, 5 kG, and 10 kG using ZEEMAN (Landstreet 1988) based on a model Fe II line, and assuming a homogeneous iron abundance. Details about the line data are presented in Appendix B. We then treated the line profiles as LSD profiles, added synthetic noise, and used them to reconstruct the magnetic field using the ZDI code by Folsom et al. (2018). We also studied the impact of two input parameters on the reconstruction of the magnetic topology with the ZDI code: $l_{\rm max}$, setting the maximum degree of the spherical harmonic expansion describing the magnetic field, and $E_{\rm slope}$, controlling the change in slope in the entropy curve. More information about these tests can be found in Appendices C and D, along with tables gathering the results. In this discussion, we only address the WFA.

The reconstructed magnetic topology for the three values of dipolar field strengths is presented in Table B1. The magnetic topology is almost perfectly recovered for a dipole field of 500 G and 5 kG, and

Downloaded from https://academic.oup.com/mnras/article/520/3/3201/6651394 by CNRS user on 11 April 2023

very well-recovered for the 10 kG field, only departing from the true topology by less than 3 per cent. In the three cases, the obliquity angle β is well estimated within $\pm 2^\circ$. On the other hand, the dipolar magnetic field strength is slightly underestimated for a magnetic field of 500 G (by 7 per cent), with larger underestimates for larger fields (23 per cent for 5 kG and 28 per cent for 10 kG). We can conclude that the WFA enables to recover the magnetic topology very well even for a field of 10 kG. The main effect appears to be an underestimation of about 30 per cent of the polar magnetic field strength at 10 kG. Therefore, the value of $B_{\rm dip} = 6320^{+170}_{-280}$ G is underestimated by about 30 per cent, leading to a more realistic polar magnetic field strength of ~ 9 kG. This value is indeed in better agreement with the analytical estimate 9635 ± 1150 G found in Section 4.4. Regarding the magnetic field topology of V352 Peg, the poloidal component is dominant, and we find that the tangential component of the poloidal field is significantly weaker than the radial component (generally $\alpha_{l,m} > \beta_{l,m}$). The tangential components of a magnetic field are often less well-constrained than the radial component in ZDI maps based only on Stokes V observations. However, in the synthetic test in Appendix B, a stronger tangential poloidal component is reconstructed than in the observations, which suggests this is not purely a systematic error. Thus we tentatively conclude that the tangential poloidal component is weaker than the radial component, although Stokes Q and U observations could help confirm this.

A particularity of this spectropolarimetric analysis has been to tailor one line mask per spectrum on the LSD analysis. Due to the high variation of the spectral lines between the different spectra, the mask should be adapted to each spectrum for a correct computation of the magnetic field. Thus, based on one cleaned template mask, 18 masks have been generated to fit the spectral lines of the 18 spectra. The longitudinal magnetic field computation and ZDI analysis have been carried out both using one single and 18 tailored masks in order to analyse the impact and consequences of this choice on the results. The shapes of the LSD profiles are similar. The main difference is the width of the profiles. The single mask we used has been tailored to spectrum #3 (2297797), taken close to the magnetic equator, when the magnetic field is weaker. Consequently, the magnetic signature extracted from other spectra obtained 'pole-on' is underestimated. As the longitudinal magnetic field is computed from Stokes signatures according to equation (1), the change in line depth impacts the value of B_l. However, this change is very weak (points are shifted only by a few Gauss). Finally, the ZDI code run on LSD files computed from a single mask shows similar results as the one presented in Section 4.5. The parameters computed following Section 4.5.2 are not impacted by this mask change.

6 CONCLUSION

In this paper, we presented the first spectropolarimetric analysis of the magnetic CP hot star V352 Peg. With an effective temperature of $T_{\rm eff} = 11\,400$ K and gravity $\log g = 4.2$progress in the understanding of magnetism2 found with Geneva photometry in good agreement with the TIC, this is an early main-sequence star. Chemical abundances and the projected rotation velocity have been derived using the ZEEMAN code from Landstreet (1988). Chromium, iron, and titanium are found in large excess while oxygen, helium, and magnesium are depleted. We have thus reclassified the star as a B9Vp star.

Stokes I and V profiles were obtained through a LSD of the spectra. Zeeman signatures are clearly detected in all the spectra, with a clear modulation of the signature with the rotation phase due to a misalignment between the rotation and magnetic axis of the star, predicted by the Oblique Rotator Model. Stokes I profiles also show a variability revealing the presence of chemical spots on the stellar surface. The modulation is also visible in the longitudinal magnetic field strength B_l, varying with the rotation phase of the star. This variation has been used to refine the rotation period with a Lomb−Scargle periodogram. Then, using the archival observation from 2011, the rotation period could be refined even more, leading to the very good accuracy of $P_{\rm rot} = 2.63654 \pm 0.00008$ d.

ZDI implemented by Folsom et al. (2018) has been used to obtain magnetic and brightness maps of the stellar surface as well as to refine the geometrical parameters. We find $i = 62^{\circ +9}_{-7}$, $v \sin i = 35.0 \pm 1.5$ km s^{-1}, and $\beta = 91.5^\circ \pm 7.0$ in good agreement with the analytical computation. Using ZDI, the polar magnetic field strength has been estimated to be $B_{\rm dip} = 6320^{+170}_{-280}$ G, differing from the analytical value by $\sim$35 per cent. When testing for the validity of the WFA, we found that the estimate of $B_{\rm dip}$ by ZDI is underestimated by up to 30 per cent for strong fields. We thus conclude that the polar magnetic field strength of V352 Peg is close to $\sim$9 kG. This underestimation is the main effect of the WFA on the reconstructed magnetic topology. In synthetic tests of the WFA, the relative magnetic energies of the poloidal and toroidal component, as well as the dipole percentage of the poloidal field, are well recovered within 3 per cent for a 10 kG field and the magnetic field maps presented in Appendix B are very close to the true topology. We also tested the impact of the magnetic field on the reconstructed relative-line strength map of the star (see Appendix B). We find that the overall relative-line strength is well recovered. For a magnetic field strength of 5 kG and greater, regions of enhanced and reduced relative-line strength are visible. Such regions trigger relative-line strength variation of about 20 per cent with respect to the expected value. This effect, although reasonable, should be taken into account when analysing the stellar relative-line strength map.

The magnetic field topology of V352 Peg is mainly dipolar, which is consistent with usual configurations for magnetic Ap and Bp stars. The toroidal component is very weak, and the magnetic field highly non-axisymmetric with respect to the rotation axis. Surface distribution of Chromium, Iron, and Titanium have been derived. Cr and Fe seem to have similar distributions with an enhanced region located in the Northern pole and spots at latitude -20°. The surface distribution of Ti is differing, with an enhanced and large spot visible at phase 0.5.

Additional spectropolarimetric observations in linear polarization (Stokes Q and U) could enable to refine the surface distribution of these chemical elements and obtain maps of higher precision.

ACKNOWLEDGEMENTS

We thank the referee for his careful reading of the manuscript and his suggestion to modify the code of Folsom et al. (2018) to map relative line strengths. Based on observations obtained at the Canada-France-Hawaii Telescope (CFHT), which is operated by the National Research Council (NRC) of Canada, the Institut National des Sciences de l'Univers of the Centre National de la Recherche Scientifique (CNRS) of France, and the University of Hawaii. This research has made use of the SIMBAD database operated at the Strasbourg astronomical Data Center (CDS), Strasbourg (France), of NASA's Astrophysics Data System (ADS), and of the VALD database, operated at Uppsala University, the Institute of Astronomy RAS in Moscow, and the University of Vienna.

DATA AVAILABILITY

The spectropolarimetric data are publicly available in the Polarbase database at http://polarbase.irap.omp.eu.

Downloaded from https://academic.oup.com/mnras/article/520/3/3201/6651394 by CNRS user on 11 April 2023

REFERENCES

Alecian E., Villebrun F., Grunhut J., Hussain G., Neiner C., Wade G. A., 2019, in EAS Publications Series, vol. 82. p. 345
Asplund M., Grevesse N., Sauval A. J., Scott P., 2009, ARA&A, 47, 481
Bailey J. D. et al., 2012, MNRAS, 423, 328
Bailey J. D., Landstreet J. D., 2013, MNRAS, 432, 1687
Bailey J. D., Landstreet J. D., Bagnulo S., Fossati L., Kochukhov O., Paladini C., Silvester J., Wade G., 2011, A&A, 535, A25
Claret A., 2019, Tables of Limb-darkening and Gravity-darkening Coefficients for the Space Mission Gaia, 3, VI/154
Donati J. F. et al., 2006, MNRAS, 370, 629
Donati J. F., 1997, MNRAS, 291, 658
ESA, 1997, The Hipparcos and Tycho Catalogues, 1200, 222
Folsom C. P. et al., 2018, MNRAS, 474, 4956
Goncharskii A. V., Stepanov V. V., Khokhlova V. L., Yagola A. G., 1982, Sov. Astron., 26, 690
Hatzes A., Penrod G., Vogt S., 1989, ApJ, 341, 456
Hatzes A. P., 1991, MNRAS, 248, 487
Hobson M. P., Lasenby A. N., 1998, MNRAS, 298, 905
Khokhlova V. L., 1976, Sov. Astron., 19, 576
Kochukhov O., Makaganiuk V., Piskunov N., 2010, A&A, 524, A5
Kochukhov O., Lüftinger T., Neiner C., Alecian E., MiMeS Collaboration, 2014, A&A, 565, A83
Kochukhov O., Silvester J., Bailey J. D., Landstreet J. D., Wade G. A., 2017, A&A, 605, A13
Künzli M., North P., Kurucz R. L., Nicolet B., 1997, A&AS, 122, 51
Landi Degl'Innocenti E., Landolfi M., 2004, Polarization in Spectral Lines. Astrophysics and Space Science Library Vol. 307, Astrophysics and Space Science Library. Kluwer Academic Publishers, Dordrecht
Landstreet J., 1988, ApJ, 326, 967
Landstreet J. D., 2011, A&A, 528, A132
Martin A. J. et al., 2018, MNRAS, 475, 1521
Martin A. J., 2017, MNRAS, 475, 1521
Mermilliod J. C., Mermilliod M., Hauck B., 1997, A&AS, 124, 349
Michaud G., Mégessier C., Charland Y., 1981, A&A, 103, 244
Moss D., 2001, in Mathys G., Solanki S. K., Wickramasinghe D. T., eds, ASP Conf. Ser. Vol. 248, Magnetic Fields Across the Hertzsprung-Russell Diagram. Astron. Soc. Pac., San Francisco, p. 305
Neiner C., Mathis S., Alecian E., Emeriau C., Grunhut J., 2014, Proc. Int. Astron. Union, 10, 61
Pakhomov Y., Piskunov N., Ryabchikova T., 2017, in Balega Y. Y., Kudryavtsev D. O., Romanyuk I. I., Yakunin I. A., eds, Stars: From Collapse to Collapse. p. 518
Perryman M. A. C. et al., 1997, A&A, 500, 501
Petit P., Donati J. F., Collier Cameron A., 2002, MNRAS, 334, 374
Piskunov N. E., Khokhlova V. L., 1983, Sov. Astron. Lett., 9, 346
Piskunov N. E., Khokhlova V. L., 1984, Sov. Astron. Lett., 10, 187
Piskunov N. E., Kupka F., Ryabchikova T. A., Weiss W. W., Jeffery C. S., 1995, A&AS, 112, 525
Preston G., 1967, ApJ, 150, 547
Schneider F. R. N., Podsiadlowski P., Langer N., Castro N., Fossati L., 2016, MNRAS, 457, 2355
Schwarzschild M. 1950, ApJ, 112, 222
Semel M., 1989, A&A, 225, 456
Silaj J., Landstreet J. D., 2014, A&A, 566, A132
Silvester J., Kochukhov O., Wade G. A., 2014, MNRAS, 444, 1442
Skiff B. A., 2014, VizieR Online Data Catalog, p. B/mk
Skilling J., Bryan R. K., 1984, MNRAS, 211, 111
Skilling J., 1989, Maximum entropy and bayesian methods, 36, 978-90-481-4044-2
Stassun K. G. et al., 2019, AJ, 158, 138
Stibbs D. W. N., 1950, MNRAS, 110, 395
Vogt S. S., Penrod G. D., 1983, Int. Astron. Union Colloquium, 71, 379
Wade G. A. et al., 2016, MNRAS, 456, 2
Wade G. A., Bagnulo S., Kochukhov O., Landstreet J., Piskunov N., Stift M. J., 2001, A&A, 374, 265
Zechmeister M., 2009, A&A, 496, 577
Ivezic Z., Connolly A. J., VanderPlas J. T., Gray A., 2014, Statistics, Data Mining, and Machine Learning in Astronomy: A Practical Python Guide for the Analysis of Survey Data. Princeton Univ. Press, Princeton, NJ, p. 403

APPENDIX A: REFINEMENT OF THE ROTATION PERIOD

Using the MiMeS data point from 2011, we could refine the rotation period estimated using a Lomb–Scargle (LS) periodogram. Fig. A1

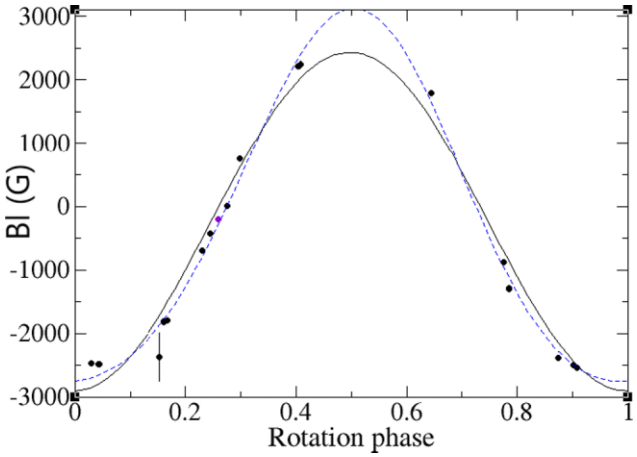


Figure A1. Longitudinal magnetic field of V352 Peg, folded in phase with $HJD_0 = 2458348.4725$ and $P = 2.63605$ d. The black and blue lines are a single-wave and a double-wave fits to the data.

represents the longitudinal magnetic field of V352 Peg as a function of the rotation phase for the period of 2.63605 d found using a LS periodogram. In Fig. A1, the data point from 2011 is located at a phase of 0.901, very close to the observation from 2018 December 21 (with a phase of 0.908) and to the single-wave and double-wave fits. However, the Stokes profiles show different signatures, which is not expected for two points relatively close in phase as can be seen from the ZDI modelling (Fig. A2). Using this, we refined the rotation period as mentioned in Section 4.3.

Downloaded from https://academic.oup.com/mnras/article/520/3/3201/6651394 by CNRS user on 11 April 2023

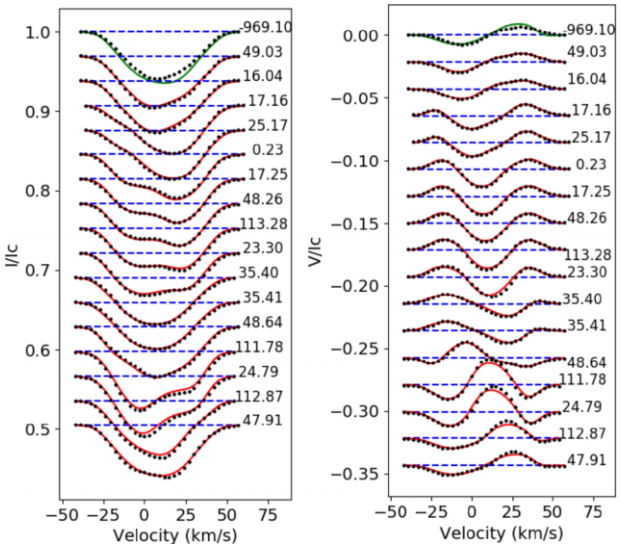


Figure A2. Comparison between observed (black dots) and simulated (red lines) Stokes I (left-hand panel) and V (right-hand panel) profiles computed with $HJD_0 = 2458348.4725$ and $P = 2.63605$ d. Stokes profiles from the MiMeS observation in 2011 are plotted in green and show that the period used here is not precise enough.

APPENDIX B: TEST OF THE VALIDITY OF THE WEAK FIELD APPROXIMATION

As mentioned in Section 5, we designed a test to check for the impact of the WFA on ZDI results. We generated synthetic-line profiles for dipolar fields with strengths of 500 G, 5 kG, and 10 kG using ZEEMAN, and then attempted to fit them using the ZDI code. ZEEMAN does not rely on the WFA and uses full Zeeman splitting calculations and polarized radiative transfer. Weaker field values are used to check the accuracy of the magnetic maps for a modest magnetic field, while the stronger field values are used to quantify the impact of departures from the WFA.

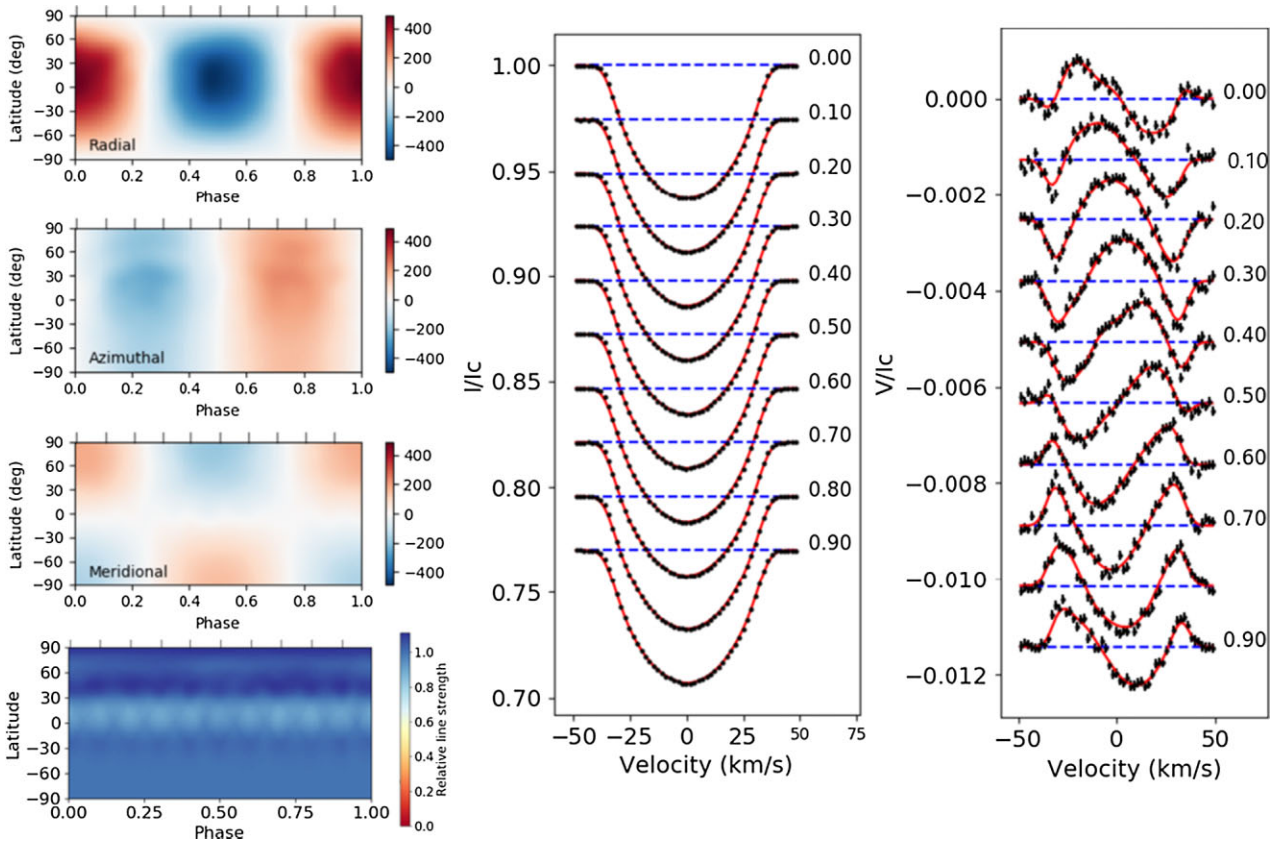


Figure B1. Left-hand panel: reconstructed magnetic field maps (three first rows) and relative-line strength (bottom row). The middle and right-hand panels show the corresponding fit to Stokes I and V profiles for an input dipole magnetic field strength of 500G.

Downloaded from https://academic.oup.com/mnras/article/520/3/3201/6651394 by CNRS user on 11 April 2023

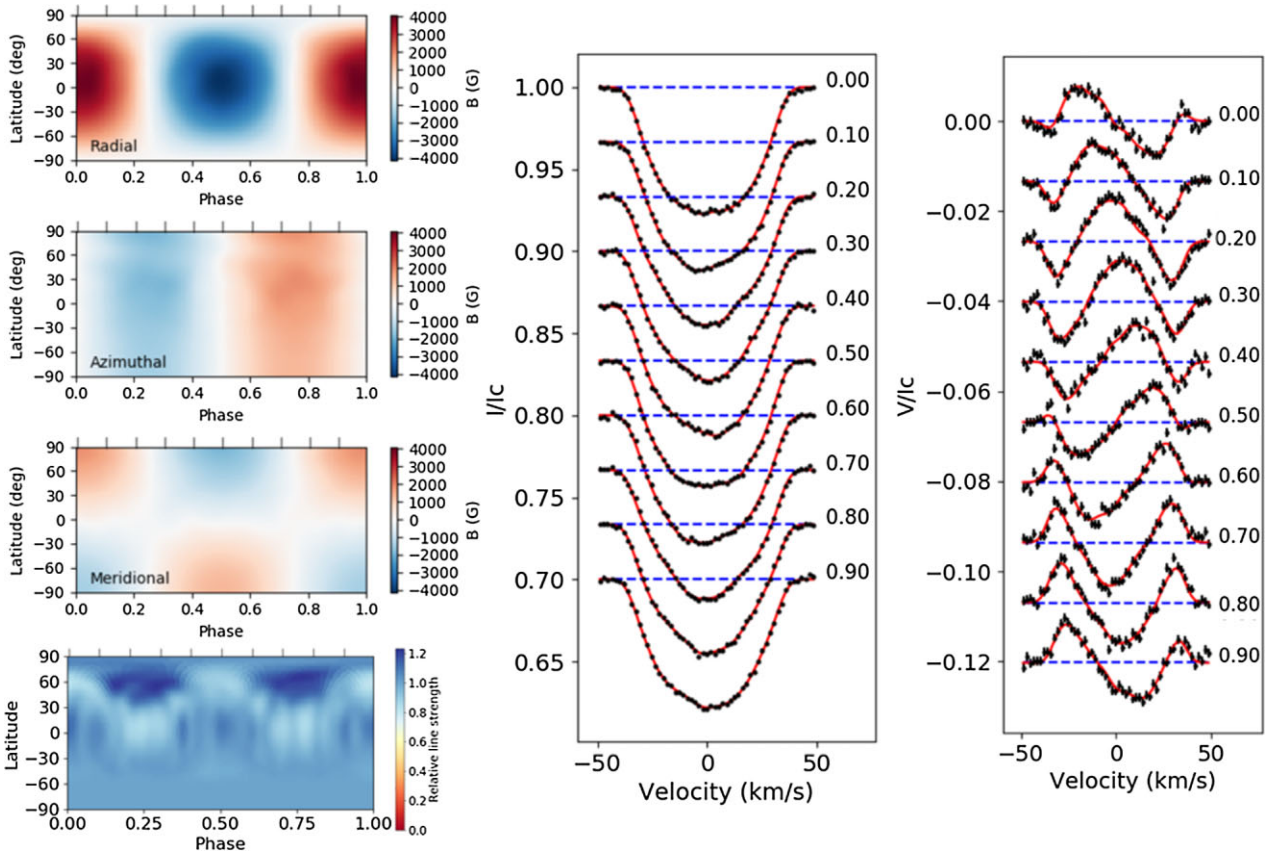


Figure B2. Same as Fig. B1 for an input dipole magnetic field strength of 5000 G.

Table B1. Reconstructed magnetic topology for different input dipolar magnetic field strengths ($B_{\rm dip}$).

Input $B_{\rm dip}$ (G)	500	5000	10000
Noise level used	0.0001	0.001	0.002
$B_{\rm dip}$ (G)	464	3847	7206
Error from true value	7 per cent	23 per cent	28 per cent
Poloidal (per cent tot)	99.7	99.7	98.2
Dipole (per cent pol)	99.5	99.3	97.4

A model Fe II line with a wavelength of 5000 Å was used in ZEEMAN along with J quantum numbers for the lower and upper levels of 1 (for a simple triplet pattern) and Landé factors for the lower and upper level of 1.2. The log gf was −1.0, the lower level excitation potential was 5.3 eV, and the radiative, quadratic Stark, and van der Waals damping parameters were respectively 8.3, −5.7, and −7.6. These line parameters were chosen because they are typical of a line in the visible wavelength domain for a 10 000 K star. The stellar angles are taken to $i = 60^\circ$ and $\beta = 90^\circ$. The other stellar parameters are chosen close to one of V352 Peg ($T_{\rm eff} = 10\,000$ K, $\log g = 4.5$, $v\sin i = 35$ km s^{-1}). Note that the test is very weakly sensitive to the temperature. We then added synthetic noise to the line profile. As the amplitude of Stokes V changes a lot with the field strength, we scaled the noise level with the magnetic field strength. We used a noise level of 0.0001 for 500 G, 0.001 for 5 kG, and 0.002 for a 10 kG field strength. The noise level is taken relative to the continuum (as 1σ of the Gaussian distribution).

For the ZDI reconstruction, we adopted the same $v\sin i$, i, rotation phases, line wavelength, and effective Landé factor as in the line model. The local Gaussian and Lorentzian line widths were set by fitting the Stokes I profiles through χ^2 minimization, with the final values of 4.5 and 0.2 km s^{-1}, respectively. We then ran the ZDI code on the synthetic line profiles to obtain a magnetic configuration for the three values of dipolar magnetic field. The relative magnetic energies and dipole magnetic field strength estimated using ZDI are gathered in Table B1, while magnetic and relative-line strength maps and fits to Stokes I and V profiles are presented in Figs B1–B3. These results are discussed in Section 5.

We find that the magnetic topology is very well-reconstructed for all three strengths, with a few per cent error at 10 kG, and less than 1 per cent error at lower field strengths. The magnetic field strength of the dipolar component is only slightly underestimated at 500 G (by 7 per cent), while it is more significantly underestimated at 5 kG (23 per cent) and 10 kG (28 per cent). Thus, we conclude that moderate violations of the WFA can have a moderate impact on the reconstructed field strength, which may be important for some applications, while the magnetic geometry is still robustly reconstructed.

Downloaded from https://academic.oup.com/mnras/article/520/3/3201/6651394 by CNRS user on 11 April 2023

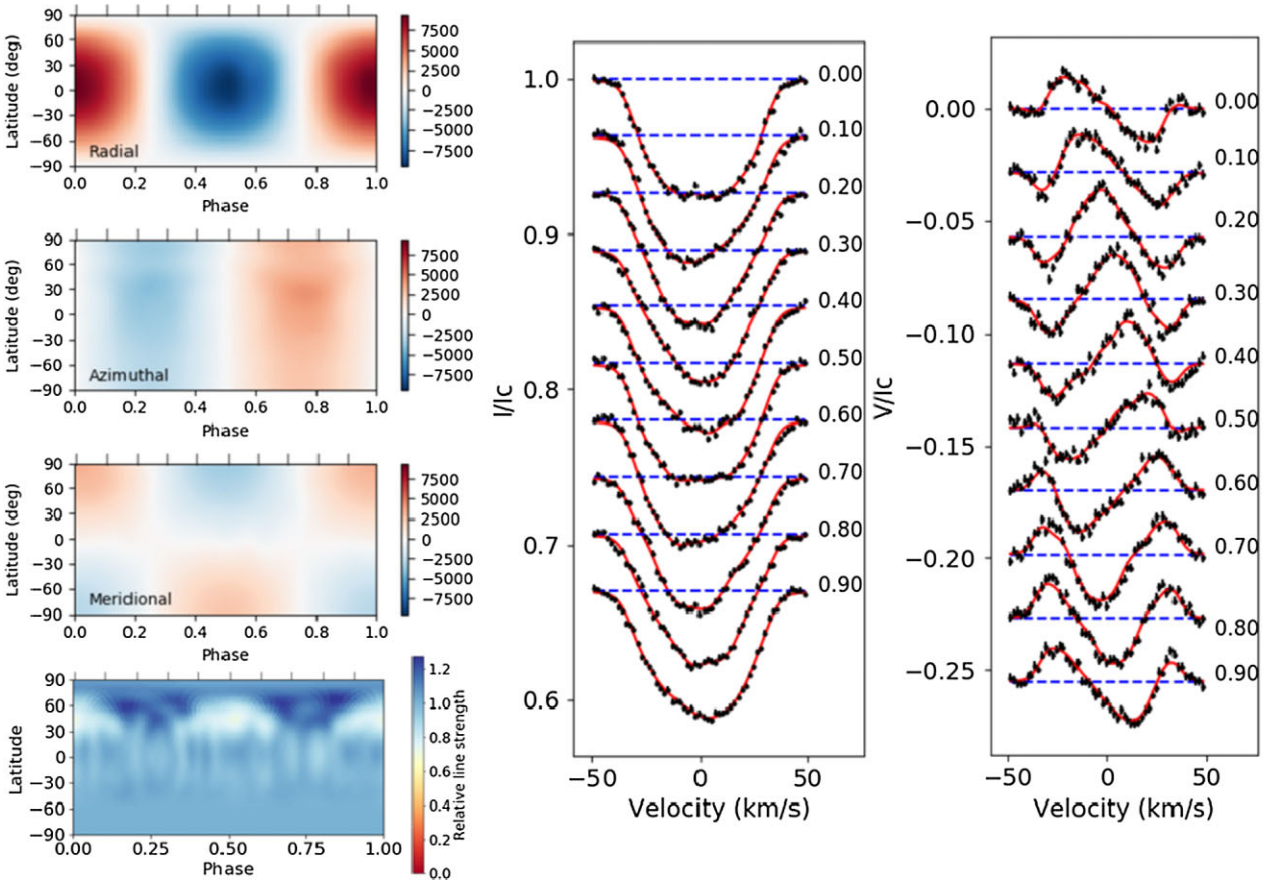


Figure B3. Same as Fig. B1 for an input dipole magnetic field strength of 10 kG.

It is also interesting to study the impact of a stronger field on the reconstructed relative-line strength map, which is supposed to be homogeneous. For a 500 G, the map in Fig. B1 is close to homogeneous, with two positive variations of +0.1 in relative-line strength at latitude 90° and 50° and an underestimation of the relative-line strength at the equatorial region. As the strength of the magnetic field increases, symmetric patterns appear in the relative-line strength map. In particular, two dark spots arise around the phases 0.25 and 0.75 at a latitude of 60°. A bright-spot is also visible between latitude 0 and 60°, moving along the stellar surface as the star rotates. For a dipole magnetic field strength of 5 kG (Fig. B2) and even for 10 kG (Fig. B3), the effect of increasing magnetic field strength in the reconstructed relative-line strength map is still moderate.

APPENDIX C: EFFECT OF THE ENTROPY SLOPE PARAMETER ON THE ZDI RESULTS

Our ZDI methodology relies on a maximum entropy regularization, and the entropy formulation requires one control parameter, which we call $E_{\rm slope}$. $E_{\rm slope}$ controls the change in slope in the entropy curve and can be defined based on equation (C1) corresponding to equation (8) of Hobson & Lasenby (1998) when $m_f = m_g = E_{\rm slope}$.

$$S[\mathbf{h}, \mathbf{m}_f, \mathbf{m}_g] = \sum_i \left(\psi_i - (m_f)_i - (m_g)_i - h_i \ln \left[\frac{\psi + h_i}{2(m_f)_i} \right] \right) \tag{C1}$$

where $\psi_i = [h_i^2 + 4(m_f)_i (m_g)_i]^{\frac{1}{2}}$.

Equation (C1) generalizes equation (2.2) of Skilling (1989) for the entropy of a positive distribution $\mathbf{f}$ to a positive/negative distribution $\mathbf{h} = \mathbf{f} - \mathbf{g}$, with $\mathbf{m}_f$ and $\mathbf{m}_g$ being two separate models for $\mathbf{f}$ and $\mathbf{g}$, acting like prior information. For the spherical harmonic description of the magnetic field, the values in $\mathbf{h}$ are the spherical harmonic coefficients α, β, and γ (e.g. Folsom et al. 2018). The real and imaginary parts of the coefficients are included as separate real terms in the summation. Here, we chose $\mathbf{m}_f = \mathbf{m}_g$ since we consider positive and negative magnetic fields with equal probability. Thus, $\mathbf{m}_f = \mathbf{m}_g = E_{\rm slope}$ and this parameter gives prior information on the distributions $\mathbf{f}$ and $\mathbf{g}$. Being directly linked to the entropy by equation (C1), $E_{\rm slope}$ influences the regularization of the magnetic field. Spherical harmonic coefficients below that value contribute less to the entropy so they are getting less strongly regularized. If the value of $E_{\rm slope}$ is too large it could lead to the regularization being too weak. On the other hand, if $E_{\rm slope}$ is too small, there is a risk of underfitting.

We used three values of entropy slope, scaled with respect to the dipolar magnetic field strength. For example, with $B_{\rm dip} = 500$ G, we took $E_{\rm slope} = 1$, 10, and 100, while we multiplied these values by a factor 10 for a field with $B_{\rm dip} = 5$ kG. We then used the ZDI code by Folsom

Downloaded from https://academic.oup.com/mnras/article/520/3/3201/6651394 by CNRS user on 11 April 2023

Table C1. Impact of the entropy slope on the reconstruction of a 500 G, 5 kG, and 10 kG magnetic field. The reconstructed field strength, error from the true value (in per cent), and percentage of poloidal and dipolar components are shown.

Field strength		500 G			5 kG			10kG	
E_{slope}	1	10	100	10	100	1000	20	200	2000
B_{dip} (G)	490	463	394	4080	3835	3243	7300	7291	6336
Error	2 per cent	7 per cent	21 per cent	18 per cent	23 per cent	35 per cent	27 per cent	27 per cent	37 per cent
Poloidal (per cent tot)	100	99.7	96.7	100	99.7	96.5	98.7	99.0	95.4
Dipole (per cent pol)	100	99.5	95.5	99.9	99.3	94.7	97.5	97.9	93.2

et al. (2018) to reconstruct the magnetic field, using the synthetic line profiles described in Appendix B. We are especially interested in the poloidal and dipolar percentage of the total magnetic energy (supposed to be 100 per cent) as well as the reconstructed dipolar magnetic field strength. We fit Stokes V profiles to a reduced $\chi^2 = 1.3$. The results are gathered in Table C1.

The trend is similar for the three magnetic field strengths. For a E_{slope} value about the same order of magnitude as the dipolar field strength, the reconstructed magnetic topology is less well-recovered than for a smaller value of entropy slope. This is because a larger E_{slope} provides a weaker constraint on the magnetic field, allowing more of the magnetic energy to be distributed in small values of higher degree spherical harmonic coefficients. In the case of a 10 kG field, we see that the poloidal and dipolar percentages increase slightly between a value of $E_{slope} =$ 20 and 200. This might be due to underfitting when $E_{slope} = 20$. The value for the entropy slope that appears to enable a good regularization without overfitting small-scale structures is about 50 times weaker than the dipolar magnetic field strength. However, this value might differ from case to case depending on the complexity of the magnetic field. For complex fields with contribution of higher-order multipoles, this value could be higher, maybe of the order of B_{dip}. V352 Peg having a simple field configuration, we used $E_{slope} = 200$ in our analysis.

APPENDIX D: EFFECT OF THE MAXIMUM SPHERICAL HARMONIC DEGREE ON THE ZDI RESULTS

Table D1. Impact of parameter l_{max} on the reconstruction of a 500 G, 5 kG, and 10 kG magnetic field.

Field strength		500 G			5 kG			10kG	
l_{max}	5	10	15	5	10	15	5	10	15
B_{dip} (G)	463	466	460	3834	3826	3814	7148	7311	7325
Error	7 per cent	7 per cent	8 per cent	23 per cent	23 per cent	24 per cent	29 per cent	27 per cent	27 per cent
Poloidal (per cent tot)	99.7	99.7	99.7	99.7	99.7	99.7	98.1	99.2	99.4
Dipole (per cent pol)	99.5	99.5	99.5	99.3	99.3	99.3	97.0	98.1	98.3

In the ZDI analysis, l_{max} is the maximum spherical harmonic degree used to compute the magnetic field based on equations (7), (8), and (9). This controls the number of free parameters used in the magnetic field inversion in ZDI. l =1, 2, and 3 correspond respectively to the dipolar, quadrupolar, and octupolar components. We tested the impact of l_{max} using the synthetic line profiles from Appendix B with three different magnetic field strengths. We reconstructed magnetic maps with $l_{max} = 5$, 10, and 15, and we fit the Stokes V profiles to a target reduced $\chi^2 =$ 1.4. The results are shown in Table D1. Overall, the value of l_{max} does not impact the reconstructed magnetic topology, especially for dipolar magnetic field strengths of 500 G and 5 kG. Modes with $l > 5$ contribute little to the reconstructed image. However, when the magnetic field reaches 10 kG, limiting the spherical harmonic degrees to 5 worsen slightly the results (by 1 per cent) than limiting them to 10 or 15. Taking this into account, using $l_{max} = 10$ appears to be a good compromise.

This paper has been typeset from a TEX/LATEX file prepared by the author.

Downloaded from https://academic.oup.com/mnras/article/520/3/3201/6651394 by CNRS user on 11 April 2023